UNIVERSITY OF HELSINKI REPORT SERIES IN PHYSICS

HU-P-D169

Interatomic potentials for fusion reactor material simulations

Carolina Björkas

Division of Materials Physics
Department of Physics
Faculty of Science
University of Helsinki
Helsinki, Finland

ACADEMIC DISSERTATION

To be presented, with the permission of the Faculty of Science of the University of Helsinki, for public criticism in the Auditorium D101 of the Department of Physics (Physicum), on November 27th, 2009, at 12 o'clock p.m.

HELSINKI 2009

ISBN 978-952-10-5642-0 (printed version)
ISSN 0356-0961
Helsinki 2009
Helsinki University Printing House (Yliopistopaino)

ISBN 978-952-10-5643-7 (PDF version)
http://ethesis.helsinki.fi/
Helsinki 2009
Electronic Publications @ University of Helsinki (Helsingin yliopiston verkkojulkaisut)

Carolina Björkas **Interatomic potentials for fusion reactor material simulations**, University of Helsinki, 2009, 51 p.+appendices, University of Helsinki Report Series in Physics, HU-P-D169, ISSN 0356-0961, ISBN 978-952-10-5642-0 (printed version), ISBN 978-952-10-5643-7 (PDF version)

Classification (INSPEC): A2852F, A3420, A6180, A6185, A7920N
Keywords (INSPEC): fusion reactor materials, molecular dynamics method, interatomic potentials, radiation damage, plasma-wall interactions, sputtering

ABSTRACT

Fusion energy is a clean and safe solution for the intricate question of how to produce non-polluting and sustainable energy for the constantly growing population. The fusion process does not result in any harmful waste or green-house gases, since small amounts of helium is the only bi-product that is produced when using the hydrogen isotopes deuterium and tritium as fuel. Moreover, deuterium is abundant in seawater and tritium can be bred from lithium, a common metal in the Earth's crust, rendering the fuel reservoirs practically bottomless.

Due to its enormous mass, the Sun has been able to utilize fusion as its main energy source ever since it was born. But here on Earth, we must find other means to achieve the same. Inertial fusion involving powerful lasers and thermonuclear fusion employing extreme temperatures are examples of successful methods. However, these have yet to produce more energy than they consume.

In thermonuclear fusion, the fuel is held inside a tokamak, which is a doughnut-shaped chamber with strong magnets wrapped around it. Once the fuel is heated up, it is controlled with the help of these magnets, since the required temperatures (over 100 million degrees C) will separate the electrons from the nuclei, forming a plasma. Once the fusion reactions occur, excess binding energy is released as energetic neutrons, which are absorbed in water in order to produce steam that runs turbines. Keeping the power losses from the plasma low, thus allowing for a high number of reactions, is a challenge.

Another challenge is related to the reactor materials, since the confinement of the plasma particles is not perfect, resulting in particle bombardment of the reactor walls and structures. Material erosion and activation as well as plasma contamination are expected. Adding to this, the high energy neutrons will cause radiation damage in the materials, causing, for instance, swelling and embrittlement.

In this thesis, the behaviour of a material situated in a fusion reactor was studied using molecular dynamics simulations. Simulations of processes in the next generation fusion reactor ITER include the reactor materials beryllium, carbon and tungsten as well as the plasma hydrogen isotopes. This means that interaction models, *i.e. interatomic potentials*, for this complicated quaternary system are needed. The task of finding such potentials is nonetheless nearly at its end, since models for the

beryllium-carbon-hydrogen interactions were constructed in this thesis and as a continuation of that work, a beryllium-tungsten model is under development. These potentials are combinable with the earlier tungsten-carbon-hydrogen ones.

The potentials were used to explain the chemical sputtering of beryllium due to deuterium plasma exposure. During experiments, a large fraction of the sputtered beryllium atoms were observed to be released as BeD molecules, and the simulations identified the *swift chemical sputtering mechanism*, previously not believed to be important in metals, as the underlying mechanism.

Radiation damage in the reactor structural materials vanadium, iron and iron chromium, as well as in the wall material tungsten and the mixed alloy tungsten carbide, was also studied in this thesis. Interatomic potentials for vanadium, tungsten and iron were modified to be better suited for simulating collision cascades that are formed during particle irradiation, and the potential features affecting the resulting primary damage were identified. Including the often neglected electronic effects in the simulations was also shown to have an impact on the damage. With proper tuning of the electron-phonon interaction strength, experimentally measured quantities related to ion-beam mixing in iron could be reproduced.

The damage in tungsten carbide alloys showed elemental asymmetry, as the major part of the damage consisted of carbon defects. On the other hand, modelling the damage in the iron chromium alloy, essentially representing steel, showed that small additions of chromium do not noticeably affect the primary damage in iron.

Since a complete assessment of the response of a material in a future full-scale fusion reactor is not achievable using only experimental techniques, molecular dynamics simulations are of vital help. This thesis has not only provided insight into complicated reactor processes and improved current methods, but also offered tools for further simulations. It is therefore an important step towards making fusion energy more than a future goal.

Contents

1 INTRODUCTION

The current population expansion and industrialization of the developing countries are inevitably leading to an increasing demand of energy. How to meet this demand is a challenging question, as the energy production of today heavily relies on resources that are on one hand nearly depleted and on the other hand polluting our planet.

At present, the primary means for producing energy is burning fossil fuels such as oil, coal and natural gas. These are non-renewable substances and the reservoirs will be drained. For instance, according to one estimate, if we continue consuming energy at the rate of year 2008, our oil reservoirs will run out in about 40 years [1]. Adding to this problem, the green-house gas carbon dioxide (CO_2) formed upon combustion is believed to affect the atmosphere, leading to changes in the global climate [2].

Fortunately, not all energy production involves non-renewable fuel, and "green energy", such as solar, wind and water power, is becoming more popular. However, these techniques currently suffer from low efficiency and require suitable construction areas. The third alternative, nuclear energy, is an efficient yet at the same time non-polluting energy source, but it does not enjoy complete public approval. The fear of catastrophic reactor accidents and/or radioactive waste is slowing down, and sometimes even stopping, the development and construction of new reactors.

There are small but undeniable risks involved in handling radioactive fuel and waste on a large scale as is done in today's nuclear reactors. These reactors are based on fission reactions, *i.e.* the process where energy is created by splitting up heavy elements into lighter elements. The opposite process, where light elements are fused together to form a heavier element releasing the excess binding energy, is called fusion. An example of this is the process where the hydrogen (H) isotopes deuterium (D) and tritium (T) form helium (He) and neutrons with an energy of 14 MeV. In this fusion reaction, no dangerous long-term radioactive waste is produced, since the half-life of the radioactive fuel component T is only 12.3 years. The exhaust of a 1 GW fusion power plant is about 250 kg of harmless He per year, which is to be compared to the 7.2×10^9 kg of CO_2 a coal plant of similar capacity produces [3].

Adding to the benefits of fusion is the abundance of fuel. There is around 33 g of D in every cubic metre of seawater and T can be generated from lithium (Li), which is a common element in the Earth's crust. Moreover, since the amount of energy released in a fusion reaction is several million times as high as in an ordinary chemical reaction, like the burning of coal, only small amounts of fuel are needed; 250 kg of fuel could run the above-mentioned fusion power plant for one year [4].

The requirements for fusion reactions are very rigorous, and unlike fission reactions, if the demands are not met, the process will simply stop, making the risk of runaway-reactions non-existing. These

specific requirements are also part of the reason why no fusion reactor that produces more energy than it consumes exists to date. The highest output/input energy gain factor (Q) has been achieved in the Joint European Torus (JET) [5], currently the largest fusion reactor in the world, reaching Q = 0.67 in 1997 [6].

In order to achieve fusion, the nuclei must be forced together despite the repulsive electrostatic Coulomb force. In thermonuclear fusion, this is realised by heating up the fuel and for the D+T reaction, temperatures around 100 million degrees are required. At these temperatures, atoms are stripped of their electrons forming a plasma. Maximizing the power output requires controlling three important plasma parameters, the temperature, the density and the confinement time, which poses a major challenge. Different devices have been developed for this purpose, the most promising being the *tokamak* (from the Russian words meaning "toroidal chamber with magnetic coils").

In a tokamak reactor, the plasma is held together by magnetic field lines in a doughnut shaped vacuum vessel [7]. Two different fields are produced so that the resulting field guides the plasma particles in never-ending loops around the torus to maximize the confinement. The high energy neutrons formed in the D+T fusion process will be absorbed in water and the water steam will run a turbine as in conventional fission-based reactors. But plasma particles will inevitably escape the confinement and either hit the walls of the reactor or be guided with possible impurities and α particles (He nuclei) to the exhaust region, called *divertor*, leading to high particle and heat fluxes at the different reactor regions.

The particle flux will cause the reactor materials to erode [8], which is undesired not only because the walls get thinner, but also because the eroded particles cause radiation losses (an increase in *bremsstrahlung* and line emission [9]) when entering the plasma. These losses depend on the eroded species, with heavier elements being more harmful. On the other hand, heavy elements are not as easily eroded as light ones, forcing compromises in the choice of plasma-facing materials (PFMs). Also, T can be trapped with redeposited materials, which is a concern from a radiological viewpoint. Examples of suitable PFMs are beryllium (Be) for the first wall and carbon (C) and tungsten (W) for the divertor region.

The material damage will be extended beyond the PFMs, since the energetic neutrons can penetrate into other parts of the reactor and also the structural materials become bombarded. The mechanical properties of these materials are altered due to radiation induced defects, and they can become brittle or start swelling [10]. Special low-activation ferritic/martensitic steels are developed purposely for being used as structural material.

If fusion is to become an economically competitive source of energy, the lifetime of a fusion reactor must be maximized [11]. Proper material selection is therefore crucial and different scenarios and materials are being tested in both existing reactors and test facilities. The plasma parameters in the next generation reactor ITER (see Fig. 1) [7], will, however, differ substantially from those possible to produce in today's reactors [12]. This makes it impossible to create the exact conditions of ITER, not to mention the ones in a full-scale power plant. A complete experimental assessment is therefore difficult to achieve, making computer simulation techniques, such as those used in this thesis, vital in providing fundamental understanding of the behaviour of a specific material in a future fusion reactor.

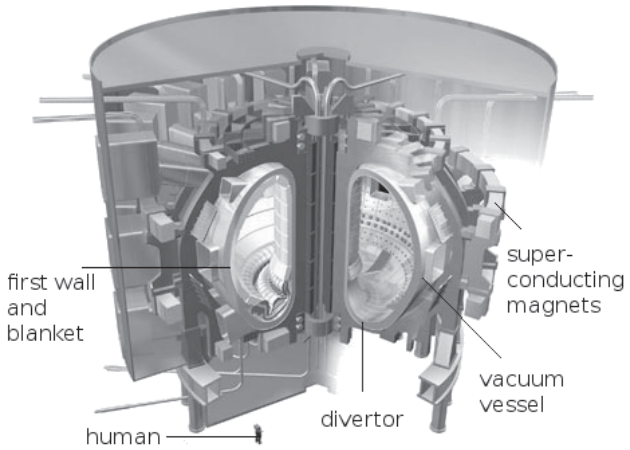

Figure 1: An illustration of the next-generation fusion reactor ITER [7] (meaning "the way" in Latin). The plasma volume is 850 m^3 and the torus major radius is 6.2 m. The goal of ITER is to achieve an energy gain factor $Q = 10$ and to produce 500 MW for a pulse of over 100 s. It is being built in Cadarache, France, and its first plasma is planned to be ignited in 2018. Figure courtesy of the European Fusion Development Agreement [4]; text added by the author.

2 PURPOSE AND STRUCTURE OF THIS STUDY

The purpose of this thesis is to improve the understanding of the response of fusion reactor materials when subject to energetic particles and harsh conditions. The methods and models developed will be of help in further studies and will assist in the selection and improvement of reactor materials.

This thesis consists of this summary and seven articles (referred to with bold Roman numbers) which are either published or under review in international peer-reviewed journals.

The structure of this thesis is as follows. In this section, the articles are summarized and the author's contribution to each of them is detailed. In the following section, all methods and models used are presented and sections 4 and 5 address the damage in the different parts of a fusion reactor. In section 6

the work is summarized, and the acknowledgements and references are found thereafter. At the end, the publications this thesis is based on are attached.

2.1 Summaries of the original publications

In publication **I**, interatomic potential models for H isotope and C interactions with Be were developed. The potential development was continued in **II** and **III** by modifying and testing potentials for iron (Fe), vanadium (V) and W. In **IV**, further testing of Fe potentials was done by comparing simulated and experimental ion-beam mixing and assessing the influence of electron-phonon coupling on simulation results of radiation damage. The effect of chromium (Cr) on radiation damage in FeCr alloys was studied in **V**, and the damage in WC alloys in **VI**. In **VII**, the erosion of Be due to a D plasma was investigated, using potentials developed in **I**.

Publication I: Interatomic potentials for Be, Be-C and Be-H, C. Björkas, N. Juslin, H. Timkó, K. Vörtler, K. Nordlund, K. Henriksson, and P. Erhart, *Journal of Physics: Condensed Matter*, **259**, 445002 (2009).

> In this study, analytical bond-order interatomic potentials for molecular dynamics (MD) simulations of H isotope and C interactions with Be were developed. Density functional theory calculations were performed in order to construct an extensive fitting database, and testing of the transferability of the potentials included melting, quenching and sputtering simulations. The potentials model bulk Be, Be defects and the Be self-sputtering process reasonably and the only observed phase of Be-C, the ionic antifluorite Be_2C, is well described.

Publication II: Comparative study of cascade damage in iron simulated with recent potentials, C. Björkas and K. Nordlund, *Nuclear Instruments and Methods in Physics Research B* **259**, 853-860 (2009).

> In order to make them better suited for radiation damage simulations, the short-range part of two recently developed Fe potentials was modified in this study. The modifications were fitted to the experimental displacement threshold energy. Comparisons of the cascade damage as predicted by the two potentials, as well as a third somewhat older potential, showed only a small scatter in the results. The previously large uncertainties regarding the damage description of different Fe potentials could therefore be reduced.

Publication III: Modelling radiation effects using the ab-initio based tungsten and vanadium potentials, C. Björkas, K. Nordlund, and S. Dudarev, *Nuclear Instruments and Methods in Physics Research B*, **267**, 3204-3208 (2009)

In this study, the high energy part of a W and a V potential was modified to correctly reproduce the experimental displacement threshold energy. Using the potentials, the clustering and total amount of post-cascade defects in W and V was compared to that in Fe, and properties affecting the outcome of a cascade were identified.

Publication IV: Assessment of the relation between ion beam mixing, electron-phonon coupling, and damage production in Fe, C. Björkas and K. Nordlund, *Nuclear Instruments and Methods in Physics Research B* **267**, 1830-1836 (2009).

The impact of electronic effects on cascade damage in iron was investigated in this study. The strength of the electron-phonon coupling (EPC) was estimated by comparing experimental and simulated values of ion beam mixing (IBM). It was found that both the choice for minimum energy at which to apply electronic stopping and the EPC strength parameter affect the amount and structure of the damage. One Fe potential was also shown to be unsuitable for IBM simulations due to its high melting point.

Publication V: Simulation of displacement cascades in $Fe_{90}Cr_{10}$ using a two band model potential, C. Björkas, K. Nordlund, L. Malerba, D. Terentyev, and P. Olsson, *Journal of Nuclear Materials* **372**, 312-317 (2008).

A two-band model (2BM) potential that reproduces the behaviour of the heat of mixing in FeCr alloys, as revealed by *ab initio* calculations and experiments, was used to model primary damage in $Fe_{90}Cr_{10}$. Large differences in the Cr content in defects were found when comparing results of the 2BM with those of other potentials. The change in short-range order due to the cascades was found to be zero within the 2BM, which is consistent with the heat of mixing at this Cr concentration. By removing the contribution of the second band in the 2BM potential, it was shown that cascades can induce phase transformations, here seen as Cr segregation. Overall, the amount and clustering of defects were the same in $Fe_{90}Cr_{10}$ as in pure Fe.

Publication VI: Major elemental asymmetry and recombination effects in irradiated WC, C. Björkas, K. Vörtler, and K. Nordlund, *Physics Review B (Rapid Communication)* **74**, 053514 (2006).

Radiation damage in the mixed WC alloy was studied with MD. It was seen that a large fraction of the resulting defects were isolated C defects and that defect recombination in WC is similar to metals. The elemental asymmetry was ascribed to large differences in defect formation energies. Since single defects move faster than clustered ones, the results indicate that the C defects can easily migrate to grain boundaries or surfaces. This can also be applied to other alloys where large differences between the defect formation energies of the constituents can be found.

Publication VII: Chemical sputtering of Be due to D bombardment, C. Björkas, K. Vörtler, K. Nordlund, D. Nishijima and R. Doerner, *New Journal of Physics*, submitted for publication.

> Chemical sputtering was observed when exposing Be to a D plasma in the PISCES-B facility. A large fraction of the sputtered Be atoms were part of BeD molecules at low energies and this fraction was seen to decrease with increasing D ion energy. The chemical effects are considerable, since $\sim$80% of the total sputtered Be comprised of Be in BeD molecules at low ion energies. The same trend was observed in simulations and the underlying process was identified as the swift chemical sputtering (SCS) mechanism. The SCS has previously been considered important only in covalently bonded materials and not in metals like Be.

2.2 Author's contribution

The major part of the development and testing of the potentials in publication **I** was performed by the author of this thesis, the exceptions being the Be-H potentials and the *ab initio* calculations. She also wrote most of the publication, except for a few paragraphs in the Method section and Appendix B.

The author set up and carried out all of the simulations and the analysis of the results in publication **II**. The modifications to one of the potentials (the MEA) were done by K. Nordlund. The major part of the text was written by the author of this thesis.

All the simulations and analyses in **III** were carried out by the author, but the density functional theory calculations were done by S. Dudarev. The publication was written by the author.

In **IV**, the author performed the simulations and the analysis and wrote the text in its entirety.

All the simulations and analyses in **V**, except for those using the CWP potential, were done by the author. She also wrote most of the publication.

The author performed the analysis of the results in **VI** and supervised the simulations that were carried out by K. Vörtler. In addition, the author wrote most of the publication.

The author carried out all the simulations and analyses in **VII**. The experimental work was performed by R. Doerner and D. Nishijima at the University of California in San Diego, USA. The author wrote the publication, apart from the experimental section.

3 MODELLING WITH MOLECULAR DYNAMICS

The ideal way of testing how a material will behave in future fusion reactors like ITER would be to perform extensive testing in surroundings that are similar to those in the reactor. A natural laboratory would then be either a present fusion or fission reactor. However, these are not adequate testing facilities due to several reasons. Firstly, the plasma parameters of ITER will enter an entirely new domain compared to the smaller reactors of today, and it is unclear how the extrapolation should be carried out. Secondly, the fission neutron spectra are completely different from fusion ones due to the lack of the 14 MeV neutrons [12].

Due to the above-mentioned reasons, proper and/or extensive testing of the effects of neutron damage and transmutation products in materials is therefore not feasible in current laboratories. However, computers can work as *virtual laboratories*. They provide insight into processes inaccessible to experiments by for instance enabling accurate calculations of properties of systems with a small amount of atoms and simulations of irradiation processes on the atomic-level.

In this section, the computer simulation methods that have been used in this work are described. The concept of molecular dynamics is explained and the interatomic potentials needed for the simulations are detailed. The specific features of each potential and approaches that are especially important for irradiation simulations are also described.

3.1 Molecular dynamics

Molecular dynamics (MD) is a method to follow the evolution of a system of particles by numerically solving equations of motion. Since its first implementation in the 1950's [13], the areas of applications of MD have increased immensely thanks to growing computational power. For example, far-from equilibrium processes such as cascades following particle irradiation are nowadays commonly modelled with MD. As an example of MD system sizes and time scales, one of the simulations in publication **IV** was a cascade event in a system containing 60 million atoms. This event took about 36 hours to simulate, using 2000 processors, and the simulated time was only 40 ps.

Although seemingly limited in time, the MD technique can be considered efficient, since the computational time scales linearly with the number of atoms in the simulation. Other methods, such as different Monte-Carlo (MC) algorithms based on random sampling and probabilities, must be used for simulations that take longer than microseconds. On the other side of the efficiency scale are *density functional theory* (DFT) methods, which can only model up to a few hundreds of atoms. DFT can achieve high accuracy when calculating the ground state energy of a given system by setting out from

the Shrödinger equation and using only a few approximations. A *multi-scale* approach, *i.e.* combining computer simulation methods on many different levels, is often advantageous.

MD has its basis in statistical mechanics: The time average of a quantity during a simulation of a system in equilibrium equals the statistical ensemble average of the quantity. (An example of an ensemble is the canonical one, where the temperature, volume and number of particles in the system are held constant.) This is true only if the so called *ergodic hypothesis* holds, meaning here that the sampling of the system during the simulations must be done so that its natural evolution is captured [14].

MD can be based on quantum-mechanical interactions, but the simulations used in this work are classical. In classical MD, the electronic subsystem and nuclei are separated based on the Born-Oppenheimer approximation [15], which states that the electrons move so fast that they reach equilibrium long before the nuclei do. The atoms are treated as objects without any internal structure, and electronic effects like the formation of atomic bonds are included in the interatomic potential that is used. At situations far from equilibrium, additional electronic effects must be included. An example of how this is done is given in Sec. 3.6.2.

In classical MD, the movements of the atoms are evaluated using for instance Newton's equation of motion. According to this, the force $\mathbf{f}_i$ acting on an atom i, with a mass m_i, results in an acceleration $\mathbf{a_i}$:

$$\mathbf{a}_i = \frac{\mathbf{f}_i}{m_i}. \tag{1}$$

The force is calculated through the gradient of the potential energy V with respect to its coordinate $\mathbf{r}_i$,

$$\mathbf{f}_i = -\nabla_{\mathbf{r}_i} V. \tag{2}$$

These equations are solved numerically by using suitable efficient integrator algorithms. The Gear 5 predictor-corrector algorithm [15] is employed in the MD code PARCAS [16] which was used in this work, so that the positions and velocities of all atoms are obtained in a step-wise manner. First, the new (predicted) positions $\mathbf{r}_i^p(t+\Delta t)$, velocities $\mathbf{v}_i^p(t+\Delta t)$ and accelerations $\mathbf{a}_i^p(t+\Delta t)$ at time $t+\Delta t$ are computed. For instance, the positions are obtained according to

$$\mathbf{r}_i^p(t+\Delta t) = \mathbf{r}_i(t) + \mathbf{v}_i(t)\Delta t + \frac{1}{2}\mathbf{a}_i(t)\Delta t^2 + \frac{1}{6}\mathbf{b}_i(t)\Delta t^3 + \frac{1}{24}\mathbf{c}_i(t)\Delta t^4 + \frac{1}{120}\mathbf{d}_i(t)\Delta t^5, \tag{3}$$

where **b**, **c**, **d** are the third, fourth and fifth time derivative of the position, respectively. Then, the forces and accelerations $\mathbf{a}_i^c(t+\Delta t)$ are calculated at the new positions. After this, the difference

between the two acceleration evaluations, $\Delta\mathbf{a}_i = \mathbf{a}_i^c - \mathbf{a}_i^p$, is used in correction terms to obtain corrected positions and velocities.

Care must be taken when choosing Δt; if it is too long, the energy is not conserved, but shortening it increases the computational time. Therefore, an adaptive time step is used in PARCAS so that Δt becomes shorter when energetic particles are present and longer during near-equilibrium simulations. A typical value is a few tenths of a femtosecond.

The total potential energy of a system of N atoms can be expressed as [15]

$$V_{TOT} = \sum_i V_1(\mathbf{r}_i) + \sum_i \sum_{j>i} V_2(\mathbf{r}_i, \mathbf{r}_j) + \sum_i \sum_{j>i} \sum_{k>j>i} V_3(\mathbf{r}_i, \mathbf{r}_j, \mathbf{r}_k) + \ldots, \tag{4}$$

where V_1 is the potential energy due to external forces, V_2 the pair potential energy which only depends on the distance $r_{ij} = |\mathbf{r_i} - \mathbf{r_j}|$ between atom i and j, and V_3 is a three-body term. Potential energy functions which include other than pair-type terms are called many-body potentials. These are more time demanding but also more flexible than simple pair potentials. In this thesis, many-body potentials of *embedded atom method* (EAM) [17] and *analytical bond-order* (ABOP) [18, 19] type are employed.

When modelling high energy particles, the potential energy function must correctly describe the repulsive interactions at small distances. This part is seldom included in the potential development, since equilibrium properties used in the fitting are not affected by it. Modifications can, however, be made after the initial fitting, as described in Sec. 3.4.

3.1.1 Controlling the temperature and pressure

Since it is often necessary or desired to use temperature (T) or pressure (P) as variables in MD simulations, one must be able to control these quantities. To model infinite systems, although only performing simulations in small cells, the T at the cell borders is often controlled to mimic heat distribution to surrounding atoms. If heat is not removed this way, unphysical heating of the system can occur during irradiation events.

In the PARCAS code, the temperature control is realised by applying the method developed by Berendsen *et al.* [20]. Here, the T of a system is controlled by coupling it to an external heat bath of desired temperature T_0. This is done by including a friction term into the equation of motion (Eq. 1), yielding

$$m_i\mathbf{a}_i = \mathbf{f}_i - m_i\gamma(\frac{T_0}{T} - 1)v_i \tag{5}$$

where v_i is the velocity of particle i and γ is the damping constant.

Since the temperature of a system is defined by the velocities of the particles in it, the temperature control is realised by scaling the velocities every time step Δt. A multiplication factor is used:

$$\lambda = \sqrt{1 + \frac{\Delta t}{\tau_T}\left(\frac{T_0}{T} - 1\right)}, \tag{6}$$

where $\tau_T = (2\gamma)^{-1}$ is a time constant determining the scaling rate. The pressure is controlled in the same manner, but here, a scaling of the atom coordinates and the simulation cell dimensions is done by multiplying them with

$$\mu = \sqrt[3]{1 - \frac{\Delta t}{\tau_P}(P_0 - P)}, \tag{7}$$

where P_0 is the desired pressure and τ_P is the time constant as in the temperature control.

During the recoil collision cascade simulations in publications **II-VI**, the temperature of the border atoms in the simulation cell was scaled to room temperature. In the bombardment simulations in **I** and **VII**, the border control was done during the first 2 ps of the run, and thereafter the whole cell was held at room temperature. Pressure control was applied prior to the cascades and bombardments, in order to let the simulation cells relax to zero pressure to find their correct dimensions at the chosen temperature.

3.2 Analytical bond-order potentials

The outcome of an MD simulation is clearly dependent on the potential that is used (see Eq. 2). Consequently, developing potential models that are able to authentically model the system of interest is vital. The development starts with finding a general functional form for V_{TOT} containing adjustable parameters [21], which are then fitted to experimental or *ab initio* data of different relevant structures. This includes cohesive energies and lattice parameters of bulk structures, molecule data and/or defect energies. Having found parameters which reproduce the fitting database, tests must be done to check whether or not the potential performs well in reproducing properties not included in the fitting. If not, the parameters are adjusted and new transferability tests are done. Several iterations are often necessary.

The potential formalism used for the Be-C-H system in this thesis is of the analytical bond-order potential type. This formalism was also used for modelling pure Fe in the potential by Müller *et al.* [22], here denoted MEA, which was used in part of the Fe simulations in this work. The ABOP

is based on Abell's and Pauling's bond-order concept [23, 24], which relates the bonding strength between two atoms to their number of neighbours: the more neighbours, the weaker the bond. The scheme resembles the tight-binding [25] scheme and with certain parameters, it has been shown to be equivalent to the EAM formalism. It can be applied to metals, covalently bonded materials as well as to ionic compounds. Further assets of the ABOP is its reactivity; it can describe breaking and formation of bonds, which is especially important in any system where chemical reactions occur and where transformations between structures of different coordinations take place.

The total energy E of a system in the Albe ABOP formalism [19] which is a modification of the Tersoff [18] and Brenner [26] ones, is expressed as a sum of individual bond energies:

$$E = \sum_{i>j} f_{ij}^c(r_{ij}) \left[V_{ij}^R(r_{ij}) - \underbrace{\frac{b_{ij}+b_{ji}}{2}}_{\overline{b_{ij}}} V_{ij}^A(r_{ij}) \right]. \tag{8}$$

V_{ij}^R and V_{ij}^A are the repulsive and attractive terms, respectively. These are pair potentials,

$$\begin{aligned} V^R(r) &= \frac{D_0}{S-1} \exp\left(-\beta\sqrt{2S}(r-r_0)\right), \\ V^A(r) &= \frac{SD_0}{S-1} \exp\left(-\beta\sqrt{2/S}(r-r_0)\right), \end{aligned} \tag{9}$$

where D_0 and r_0 are the bond energy and length of the dimer molecule, respectively, and S and β are adjustable parameters. Through the cut-off function f_{ij}^c the interaction range is restricted, usually to nearest neighbours only,

$$f^c(r) = \begin{cases} 1, & r \le R-D, \\ \frac{1}{2} - \frac{1}{2}\sin\left(\frac{\pi}{2}(r-R)/D\right), & |R-r| \le D, \\ 0, & r \ge R+D. \end{cases} \tag{10}$$

Here, R and D are parameters determining the cutoff range and interval. b_{ij} in Eq. 8 is the bond order term, which includes three-body interactions and angularity,

$$b_{ij} = (1+\chi_{ij})^{-\frac{1}{2}}, \tag{11}$$

where

$$\chi_{ij} = \sum_{k(\neq i,j)} f_{ik}^c(r_{ik}) g_{ik}(\theta_{ijk}) e^{2\mu_{ik}(r_{ij}-r_{ik})}. \tag{12}$$

μ_{ik} is a fitting parameter and the angular function g_{ik} is of the form

$$g_{ik}(\theta_{ijk}) = \gamma\left(1 + \frac{c^2}{d^2} - \frac{c^2}{d^2+(h+\cos\theta_{ijk})^2}\right), \tag{13}$$

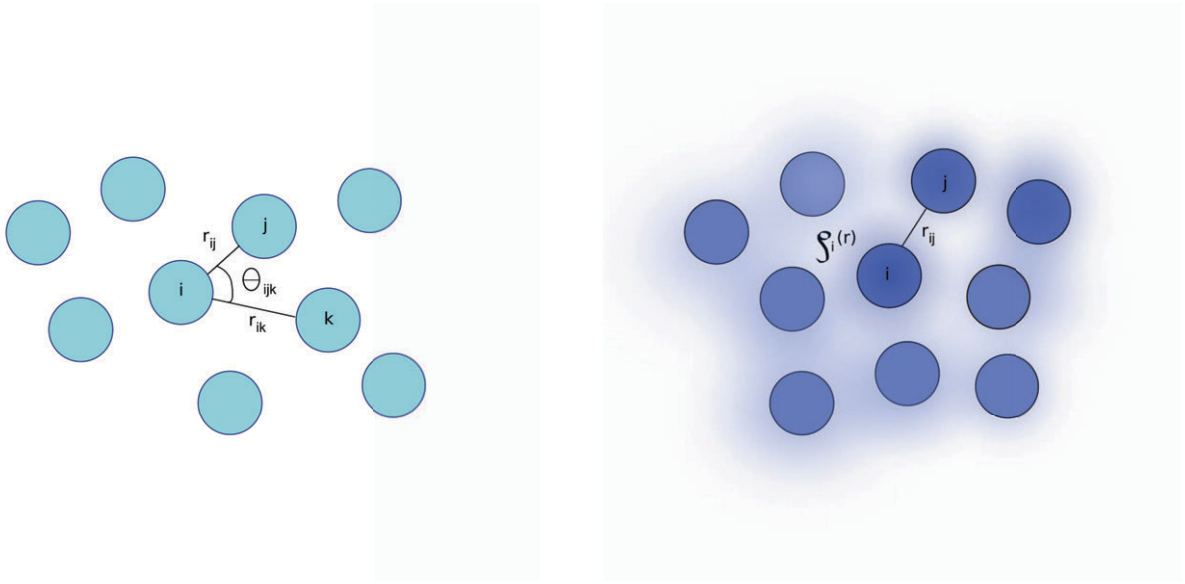

(a) (b)

Figure 2: (a) An illustration of the atoms i, j, k and the angle θ_{ijk} used in Eq. 12 for the ABOP formalism. In (b), the electron density ρ that is essential for the EAM potential formalism is schematically shown.

where γ, c, d and h are alterable parameters. The definition of θ_{ijk} and r is illustrated in Fig. 2(a).

3.2.1 ABOPs for the Be-C-H system

As a first step into modelling the complete Be-C-W-H system, a pure Be potential must be developed. This was done in publication **I**, where two Be potential versions (Be-Be I and Be-Be II) were parameterized. Version I is intended for pure Be simulations, and the second version works excellently together with the Be-C potential. How well these two potentials reproduce the bond lengths and energies of different Be structures used in the fitting is illustrated as a so called Pauling plot in Fig. 3. Owing to its completely filled subshells ($1s^2 2s^2$), the Be_2 dimer is very weakly bonded and has a large bond length and is therefore not reproducible within the ABOP formalism. Here, the bond energy namely decreases and the bond length increases with coordination number, forcing the dimer to have the strongest energy per bond and shortest bond length and is thus situated in the top left corner in Fig. 3.

The properties of bulk Be in its ground state, the hexagonal close-packed structure, are, on the other hand, well described within both potentials versions. In addition to structural parameters, these include the melting point, the elastic constants and the bulk moduli. Also, the most stable interstitial configuration, the basal-octahedral, could be reproduced, although having a slightly smaller forma-

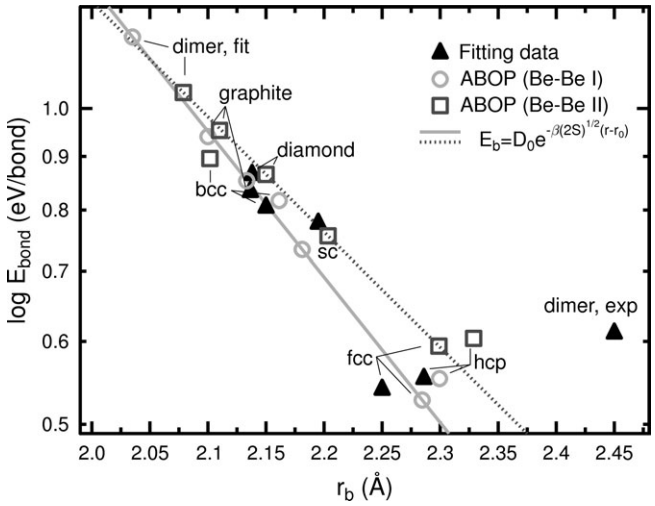

Figure 3: Semilogarithmic plot of the energy-bond relation for different beryllium phases. The circles show values predicted by the analytical bond-order potential (ABOP), Be-Be I, the squares are the Be-Be II potential, and the lines are the Pauling relation with parameters of each version. From publication **I**.

tion energy compared to DFT calculations. The surface energies are also well described. A drawback of the Be potentials is a negative thermal expansion at high temperatures.

Only one phase has been experimentally observed in the Be-C system, the ionic antifluorite Be_2C structure, Fig. 4(a). Very little is known about this structure, making the benchmarking of the Be-C potential difficult. The short-ranged character of the ABOP scheme could also add to the difficulties of encapsulating ionic interactions that are long-ranged, but it has been shown by extensive testing that the ABOP formalism is adequate for mimicking ionic systems such as gallium nitride even without additional long-range or charge-transfer terms [27]. And indeed, the Be-C potential developed here captures the properties of bulk Be_2C well.

Testing of the Be-C potential included quenching simulations to ensure that no false minima appear. When cooling a random melt with a Be:C ratio of 2:1 from a high temperature to 0 K, the antifluorite structure was formed as seen in Fig. 4(b), confirming that the potential correctly predicts the structure of BeC at this concentration and that no deep false minima are present. When the ratio was 1:1, the melt segregated into regions of three-fold coordinated C and Be_2C (see Fig. 4(c)). Bombardment of Be with C ions resulted in layers of Be_2C on the surface, indicating that the potential is capable of studying mixed material formation (see Sec. 5).

The Be-H potential was fitted to properties of BeH_x molecules and to H as an interstitial defect in bulk Be. Since the isotopes D and T react chemically in the same way as H, their interaction with Be can be modelled with this potential as well, keeping in mind the mass differences.

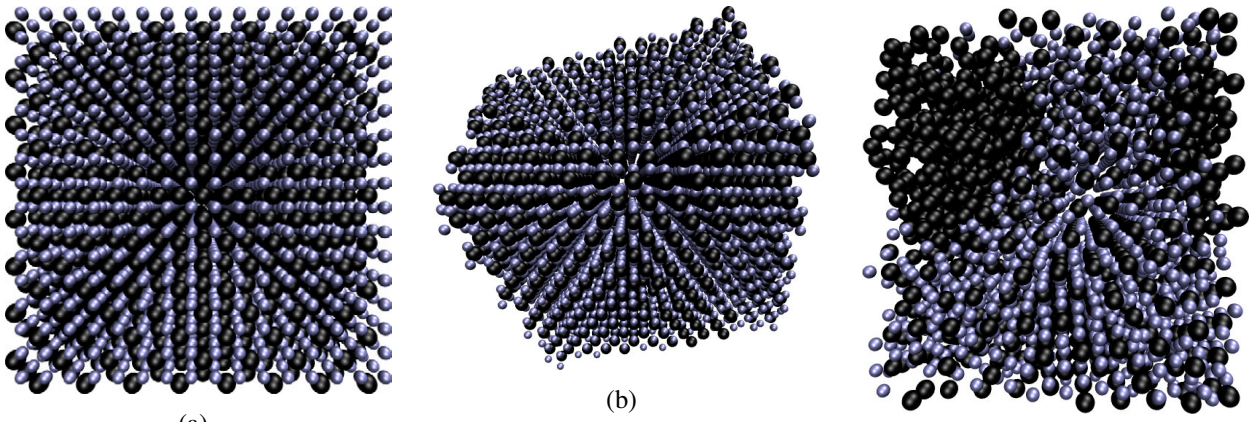

(a) (b) (c)

Figure 4: (a) The ideal antifluorite Be_2C structure. The black spheres represent carbon atoms. (b) The final structure after quenching from 4000 K to 0 K at a rate of 0.5 K/ps with a ratio Be:C = 2:1 in the initial melt. Both (a) and (b) illustrate the antifluorite structure; (c) The final structure after quenching a random melt with Be:C = 1:1. Regions of amorphous three-fold coordinated carbon and Be_2C are seen. From publication **I**.

3.3 The embedded atom method

The embedded-atom method (EAM) formalism is a model that is especially suited for modelling of metals. Here, the main part of the attractive energy in the system is described by a so-called embedding term F, aiming at mimicking the way the metal nuclei are embedded in a sea of electrons (see Fig. 2(b)). The term can for instance be determined with the help of the second-moment approximation of the tight-binding theory of solids [28], resulting in the Finnis-Sinclair solution [29]:

$$F(\rho_i) = -A\sqrt{\rho_i}, \tag{14}$$

where A is a fitting parameter and ρ_i is the electron density at atom i. The total energy of a system is in EAM type potentials

$$E = \sum_i F\left[\sum_{j\neq i}\rho_i(r_{ij})\right] + \frac{1}{2}\sum_{i,j(j\neq i)} V_{ij}(r_{ij}), \tag{15}$$

where $V_{ij}(r_{ij})$ is a two-body term. In this thesis, the following EAM-like potentials were employed. For pure Fe, three different potentials were used: One developed by Ackland *et al.* [30], denoted AMS, one magnetic potential by Dudarev *et al.* (DD) [31], and one by Chakarova *et al.* (CWP) [32]. In Ref. [32], Chakarova *et al.* also developed one of the two potentials for Fe and Cr interactions that were used here. The two-band model (2BM) by Olsson *et al.* [33] is the other, in which Fe-Fe interactions are modelled with the AMS potential. The V and W potentials are also EAM-types and developed by Derlet *et al.* [34].

3.4 Adjustments of repulsive potentials

Particle irradiation processes often include high energy recoils and therefore short-distance interactions between atoms. At these ranges, typically $\lesssim 1$ Å, the repulsive forces, such as the Coloumb repulsion between two positively charged nuclei, become stronger than the chemical interactions between the electron shells. The short range part of a potential affects not only ballistic processes, but also the defects and melting properties of a material, and it is often added to a potential after ensuring that the equilibrium properties are correctly modelled. The most commonly used formula is the universal Ziegler-Biersack-Littmark (ZBL) potential V_{ZBL} [35] which contains a pure Coulombic repulsive term that is mitigated by a screening function $\phi(r)$ at larger distances,

$$V_{ZBL}(r) = \frac{e^2}{4\pi\varepsilon_0}\frac{Z_1 Z_2}{r}\phi(r/a). \tag{16}$$

Z_1 and Z_2 are the charges of the interacting nuclei, e is the elementary charge, and

$$a = \frac{0.8854 a_0}{Z_1^{0.23} + Z_2^{0.23}}, \tag{17}$$

where a_0 is the Bohr radius. The universal screening function has been constructed by fitting to the interaction energy between ions, resulting in:

$$\phi(x) = 0.1818e^{-3.2x} + 0.5099e^{-0.9423x} + 0.2802e^{-0.4028x} + 0.02817e^{-0.2016x}. \tag{18}$$

The accuracy of this potential is $\sim$10% [35].

A smooth join between the high and low-energy parts is realised with, for instance, exponential or polynomial functions containing adjustable parameters that must be fitted. The continuity of the potential functions as well as their first and second derivatives at the spline boundaries must be taken into account in the construction.

In publication **II**, the repulsive part of two Fe potentials was modified in order to reproduce the experimental threshold energy for the creation of a defect. The same was done in publication **III** for a W and V potential. The modified potentials belong to two different formalism groups: one of the Fe potentials is of the ABOP type, the MEA potential, and the other Fe potential, DD, as well as the W and V ones [34], are EAM-like potentials. Upon modification, the Fe potentials were called MEA-BN and DD-BN, respectively.

When adjusting the former kind, a new potential was constructed in the following way.

$$V_{modif}^{ABOP}(r) = V_{ZBL}(r)(1-F(r)) + V_{equi}^{ABOP}(r)F(r), \tag{19}$$

where the Fermi function

$$F(r) = \frac{1}{1+e^{-b_f(r-r_f)}} \tag{20}$$

was used and where V_{equi} equals the potential close to equilibrium. For the EAM types, the modified potentials were

$$\begin{aligned} V_{modif}^{EAM}(r) &= V_{ZBL}(r), \quad r \leq r_1 \\ &= V_{join}(r), \quad r_1 < r < r_2 \\ &= V_{equi}^{EAM}(r), \quad r \geq r_2 \end{aligned} \tag{21}$$

where V_{join} is a joining fifth order polynomial function and r_1 and r_2 define the range of the join.

The EAM density function ρ_i was also modified for the W and V potentials, in order to correctly reproduce the contribution of attractive d-states (3d orbitals in V and 5d in W) and requiring that the bonding part of the potential does not diverge at small atomic separations. The function was therefore given a saturation value at a distance where the orbitals of two atoms begin to overlap and a third order polynomial was used for a smooth join. The overlap was estimated by calculating the radial distribution of the electron density distribution by solving the relativistic Dirac equation in the local spin density approximation (see Pub. **II**).

An illustration of the adjustments of both the repulsive potential and the electron density for V and W is given in Fig. 5. How these changes reflect upon the defect threshold energy is seen in table 1.

3.5 Collision cascades

When studying radiation damage, MD methods can be used to model the primary damage, *i.e.* the damage that remains after collision cascades. These cascades are formed due to energetic particles, such as neutrons or electrons, hitting lattice atoms which then become energetic recoils producing additional collisions. Characteristic of a cascade due to a high energy recoil is a heat spike, during which a molten under-dense region in the middle and a hot high-pressure region surrounding it are formed [42, 43]. Following this heat spike and subsequent energy dissipation, the lattice starts to relax

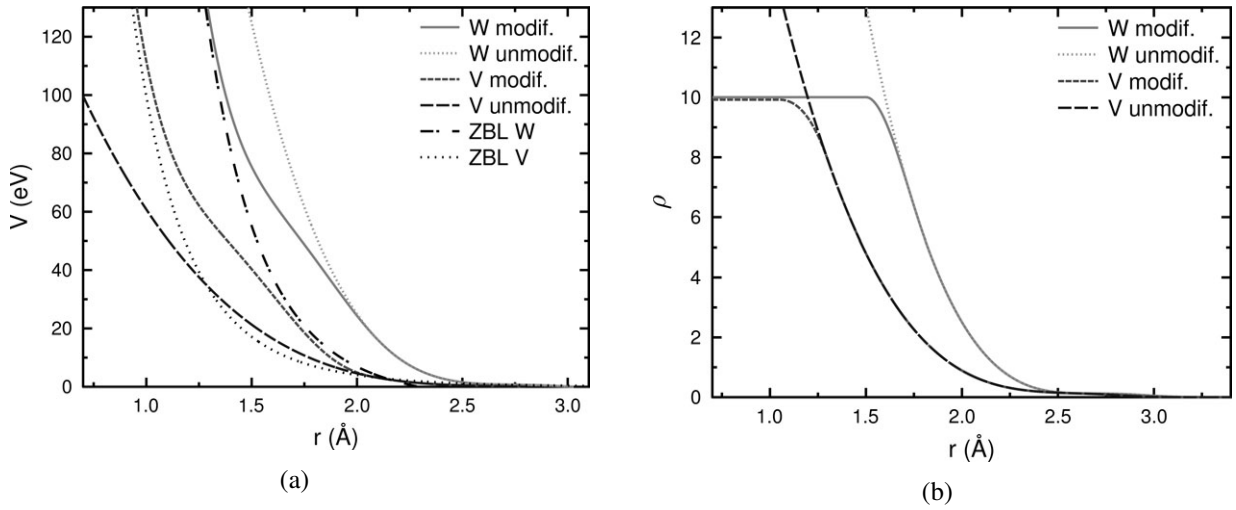

Figure 5: (a) The modification of the repulsive part of the V and W potentials in Ref. [34]. The ZBL potential is the universal potential by Ziegler *et al.* [35]. From publication **II**. (b) The electron density function modification of the same potentials.

and resolidification of the molten zone and recombination of defects take place. After some tens of picoseconds, only the so-called primary damage remains.

The primary damage consists of misplaced atoms (interstitials) and vacant lattice sites (vacancies) and clusters of these, see Fig. 6. A Frenkel pair is one interstitial-vacancy pair, and this is often used as a measure of the total amount of defects. To identify the defects, Wigner-Seitz cells centered on

Table 1: Threshold displacement energies in eV as predicted by the V and W potentials. $N_{direction}$ is the number of directions that was used in determining the minimum $E_d(\theta,\phi)$ and the average threshold $E^{av}_{d,ave}$. The uncertainty of the values (except for the average threshold) is due to the energy steps used in the calculations. The direction specific thresholds are calculated in an interval of 0.2 Miller index around the principal directions. The simulated thresholds were obtained at 4 K and 20 K for W and V, respectively. Available experimental values are also included.

		$N_{directions}$	$E_d(\theta,\phi)$				$E^{av}_{d,ave}$
			All directions	⟨100⟩	⟨110⟩	⟨111⟩	
W	Unmodif.	680	55±3	55±3	>100	93±3	88.3±0.7
	Modif.	1096	41±1	41±1	93±1	41±1	84.5±0.9
	Exp.		42±1[a] (< 7 K), 42±1[b] (4 K), 50±2[c] (350 K)	40±2[a]		44±1[a]	
V	Unmodif.	2713	13±3	13±3	19±3	13±3	19.6±1.8
	Modif.	1561	23±1	23±1	43±1	41±1	55.0±0.6
	Exp.		30[d] (295 K), 26±2[e] (4 K), 25±2[f] (20 K)	30[d]	39[d]	34[d]	

[a] Ref. [36], [b] Ref. [37], [c] Ref. [38], [d] Ref. [39], [e] Ref. [40], [f] Ref. [41]

every (perfect) lattice site are used in such a way that an empty cell corresponds to a vacancy and a doubly (or more) inhabited cell is an interstitial.

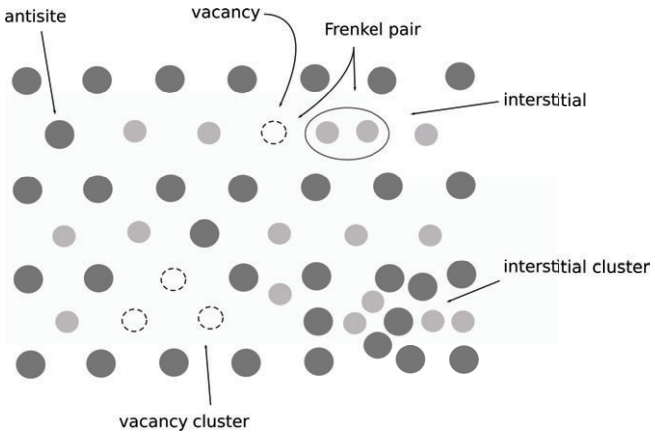

Figure 6: Illustration of the common types of lattice defects.

In this thesis, collision cascades were modelled by initiating a recoil near the middle of a simulation cell. This recoil was given a certain energy and a random direction and the temperature of the borders was controlled to room temperature. No secondary recoils were allowed to enter the border regions, since due to periodic boundaries, these could cause artificial cascade overlapping. Huge simulation cells, containing up to 60 million atoms, were therefore required for the high energy cascades. The cascade process was followed for several tens of picoseconds.

A cascade is illustrated in Fig. 7. Here, the cascade is induced by a 20 keV recoil in Fe and only the created vacancies and interstitials are shown. The resulting primary damage is seen in the last frame. Typically, vacancies are found in the middle, surrounded by interstitials.

Although the post-cascade damage is created on the picosecond scale and will be subject to considerable changes as time evolves, its initial structure is important. For instance, clusters do not necessarily migrate in the same manner or speed as isolated defects, making the long-time scale final damage dependent on the arrangement of initial defects.

3.6 Comparative studies

3.6.1 Potential models

Since no single method can be considered to be ideal or even the best one for deriving an interatomic potential, many different formalisms have been used in literature. Each formalism has its advantages and drawbacks, and therefore it is important to know which feature of a potential affects a certain

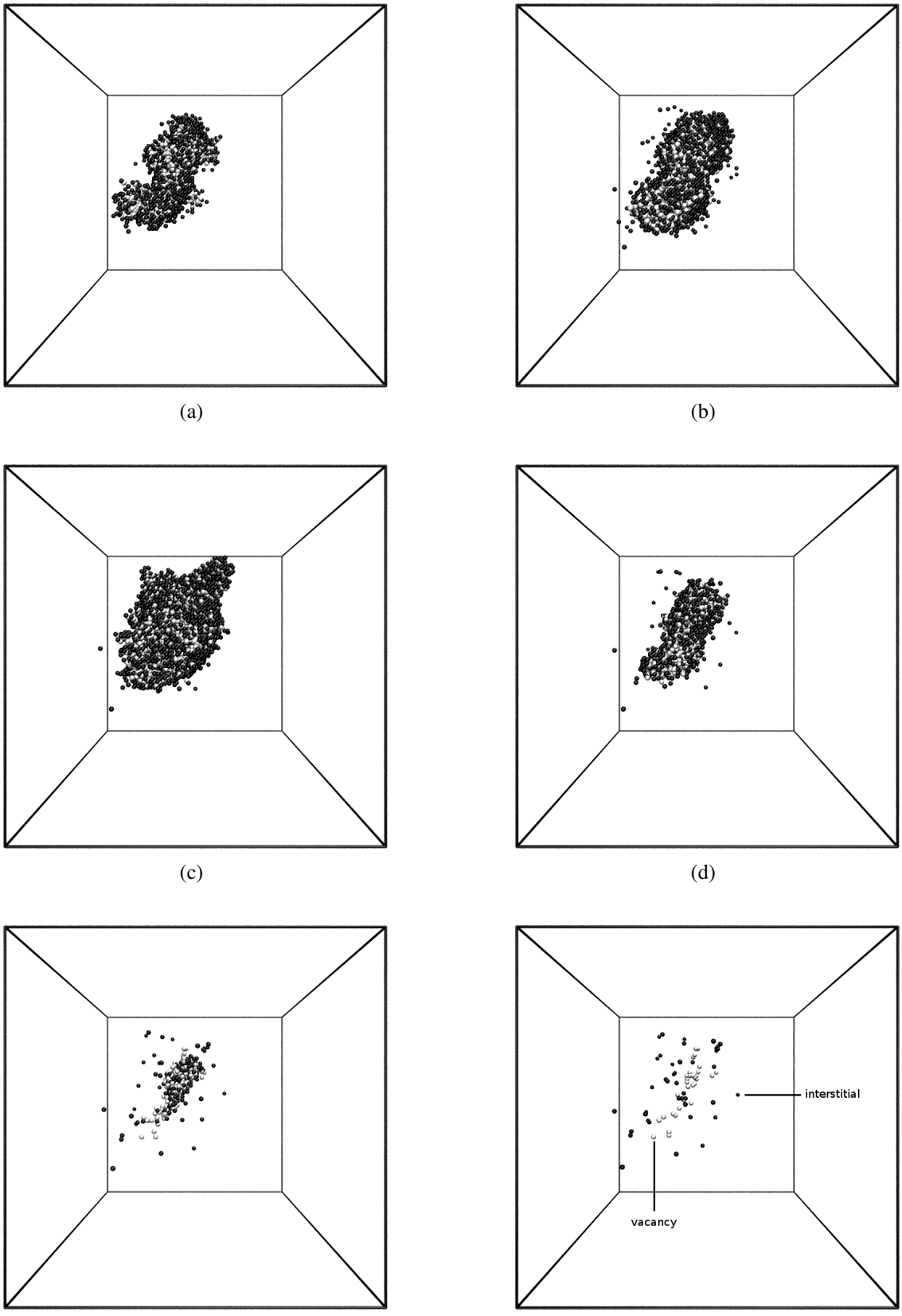

Figure 7: The time evolution of defects during a 20 keV collision cascade in Fe. (a) 0.25 ps after the initiation of the recoil, (b) 0.5 ps, (c) 1 ps, (d) 2 ps, (e) 5 ps and (f) 25 ps. In (f) only the defects (consisting of vacancies and interstitials) that have not recombined remain, representing the resulting primary damage.

part of a simulated process. This gives hints as to what basic property a potential must be able to reproduce correctly in order for the simulation results to be reliable.

Simulations of cascades with different potentials result in large variations in the structure of the primary damage, which is mainly ascribed to an incorrect description of the melting point or of interstitial energetics [44, 45]. In publication **II**, three Fe potentials based on different potential formulas but all correctly reproducing the <100> dumbbell (two atoms sharing one lattice site and situated on the same axis) as the most stable interstitial configuration [46], are compared. After modifying two of them as described in section 3.4, the variations in cascade damage are greatly reduced when compared to previous Fe potentials. As an example of this reduction, the number of created Frenkel pairs for the three potentials is plotted in Fig. 8, to which the scatter of previous potentials has been added as a shaded area.

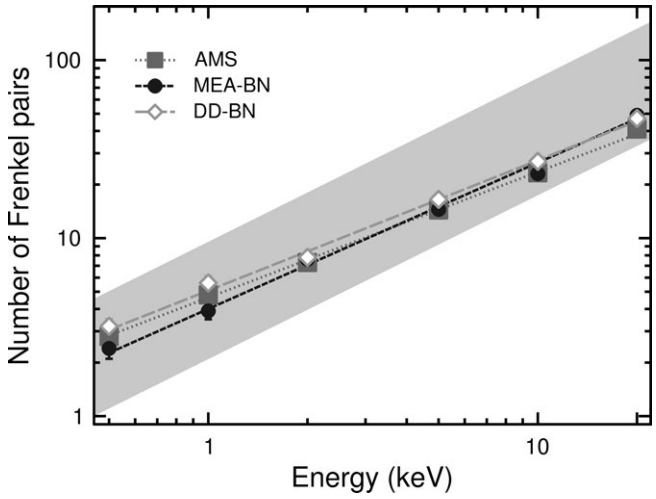

Figure 8: The average number of Frenkel pairs produced in cascade simulations in Fe using three different interatomic potentials. The shaded area shows the distribution of the amount as predicted by earlier Fe potentials.

When comparing potentials of the same formalism but applied to different elements, it is possible to recognize properties that affect the primary damage. In publication **III**, the modified V and W potentials were used in collision cascades, and the results were compared to Fe when modelled with the EAM-type potential which was modified in publication **II**, the DD-BN potential.

The Frenkel pair production at the end of the cascades was seen to be dependent on the defect formation energies: the amount was lowest in W where the formation energies are the highest. Sub-cascade formation for high energy recoils, on the other hand, affects the interstitial cluster fraction by hindering the formation of large clusters. As shown in Fig. 9(a), the fraction was seen to be the smallest in V at high energies, since due to the larger lattice constant and smaller mass of V, sub-cascades are formed more easily here than in Fe and W. The faster mobility of the most stable interstitial defect in

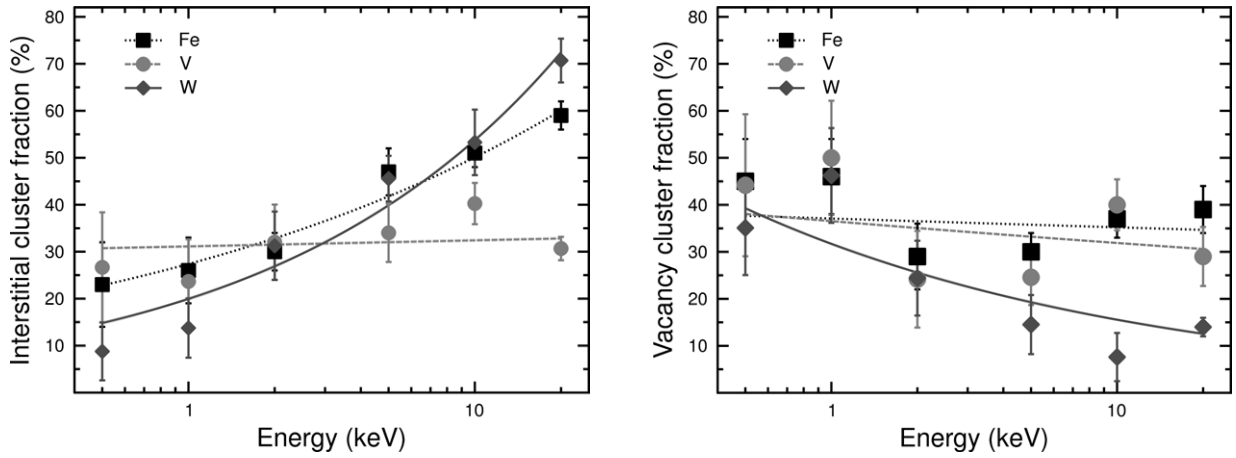

(a) (b)

Figure 9: Fraction of defects in clusters after cascades initiated by recoils of different energies. The interstitial fraction is shown in (a) and the corresponding vacancy one in (b). The data were obtained using the modified Fe, V, and W potentials. From publication **III**.

W (the <111> crowdion) when compared to the <110> dumbbell in Fe, explains why the interstitial fraction is the largest in W. A high mobility makes it possible for interstitials to find each other and form clusters.

The vacancy cluster fraction also displayed elemental variations (see Fig. 9(b)). Fe and V showed nearly a constant fraction for the whole energy range that was considered, but the fraction in W was seen to decrease with energy. This behaviour is ascribed to the higher melting point of W, since a high melting point allows the recrystallization front to push vacancies towards the center of a cascade to move faster. This, in turn, leads to the fact that the vacancies freeze in the lattice instead of migrating into the center to form clusters. At lower energies no heat-spike, and thus no recrystallization front, exists, explaining why the elemental differences are visible only at high energies.

The above discussion shows that, in order to model the primary damage properly, it is important that defect energetics and melting points are accurately reproduced within a potential.

3.6.2 Electronic effects

To further check the reliability of the description of a cascade process for a certain potential, comparisons to experiments must be done. One experimental quantity which can be directly related to cascades is the ion-beam mixing (IBM), which is the athermal relocation of atoms induced by ion irradiation [47]. Mixing crucially depends on the energy and heat distribution, implying that a correct

description of both the electronic stopping (S_e) [35] and electron-phonon coupling (EPC) [48, 49] is required.

Stopping S is the energy per length unit lost by atoms moving in a solid, $S = \frac{dE}{dx}$. For atoms with energies above $\sim$100 keV, this energy is predominantly lost to inelastic collisions with electrons and thus the stopping is electronic (as opposed to nuclear). As a result of the collisions, the electrons become excited, but are rapidly thermalized through electron-electron interactions.

EPC is the interaction between electrons and lattice vibrations. Through this, atoms can either lose or gain energy depending on their velocity and the temperature of the electronic subsystem. Since the heat conduction in metals is dominated by electronic conduction, EPC is needed to model the heat dissipation, especially at the end of a cascade, properly.

These two electronic effects can be included in an *ad hoc* manner by adding a frictional term, $m_i \gamma v_i$, to the equations of motion as described in Sec. 3.1.1. Now, the parameter γ is either the coefficient for S_e (γ_{S_e}) or for EPC (γ_{EPC}), or a combination of these. The former is calculated with the help of the ZBL stopping formula [35] and the latter equals

$$\gamma_{EPC} = m_i \alpha \frac{T_i - T_e}{T_i}, \tag{22}$$

where α represents the strength of the coupling and T_i and T_e are the atomic and electronic temperature, respectively [50]. To combine these two effects, a cut-off energy E_{min} can be included, corresponding to, for instance, the cohesive energy of the material in question. Above this, one enforces damping according to the S_e and below according to the EPC.

Including S_e in this way has been shown to be reasonably accurate [51], but the correct treatment of EPC is still an open question [52] and several different schemes have been proposed [43, 50, 53–59]. In the simulations in publication **IV**, a constant heat bath of 300 K for the electronic system is assumed, representing an infinite electronic thermal diffusivity. More sophisticated models include an electron-temperature dependent electronic heat capacity and a lattice- and electron-temperature dependent electronic thermal conductivity [59].

In publication **IV**, simulated predictions of the IBM efficiency Q in Fe were compared to experimental values obtained for 650 keV krypton (Kr) ion irradiation of Fe [47], and the influence of EPC strength and E_{min} was studied. The efficiency is experimentally defined as

$$Q_{exp} = \frac{Dt}{\Phi F_{D_n}}, \tag{23}$$

where D is an effective diffusion coefficient for mixing, t is the implantation time, Φ the ion fluence and F_{D_n} the deposited nuclear energy per unit depth. The unit of the efficiency is Å^5/eV. Using the atomic definition of the diffusion coefficient, $D = \frac{<r^2>}{6t}$, the mixing efficiency can be calculated as a function of ion energy [60]:

$$Q_{sim}(E_0) = \frac{\int_0^{E_0} R^2(E) n(E) dE}{6 n_0 E_{D_n}}, \tag{24}$$

where R^2 is the square of the total atom displacement after cascades initiated by recoils with energy E, and n_0 is the atomic density (in body-centered cubic Fe this equals $2/a_0^3$, where a_0 is the lattice constant). E_{D_n} is the deposited nuclear energy and E_0 is the energy of the bombarding ion (650 keV in this case) and $n(E)dE$ is the recoil spectrum of the Kr ions.

The Q values in Fe, as predicted by the potentials used in publication **II**, are illustrated in Figure 10(a). Agreement with the experiment was obtained only with a correct melting point combined with an EPC time constant of 1.6352 ps or E_{min} set to 1 eV. The effects of different conditions on vacancy clustering after 20 keV cascades using the AMS potential is illustrated in Fig. 10(b), showing no large variation over the range of EPC strength. The same trend was seen for interstitial clusters, but an increase in the amount of Frenkel pairs was noticeable when the coupling was strong. The reason is that EPC shortens the life-time of the cascade heat spike and single defects thus have less time to recombine.

The mixing efficiency was seen to be dependent on the melting point in a potential; a high melting point as in the MEA-BN potential results in a low mixing, and the mixing in DD-BN and AMS is higher due to a lower melting point. This is also explained by the heat spike character, as a low melting point results in a large heat spike where atoms easily mix during a cascade. The AMS is in closest agreement with the experimental temperature of 1750 K and since the MEA-BN overestimates the melting point with over 500 K, it is unsuitable for IBM simulations.

4 CHALLENGES FOR STRUCTURAL MATERIALS

Although the plasma facing materials (PFMs) are subject to the harshest conditions due to their proximity to the plasma, the requirements for structural materials supporting the basic structures of a reactor, the vacuum-vessel and the blanket, are also rigorous. Reactor structures will operate at temperatures where thermal creep (time dependent deformation) occurs and transient events will test their tensile strength, fracture toughness and fatigue properties [61, 62]. Having assured that a material in question also is compatible with the coolant (e.g. water, liquid Li) and T breeder (e.g. Li), issues

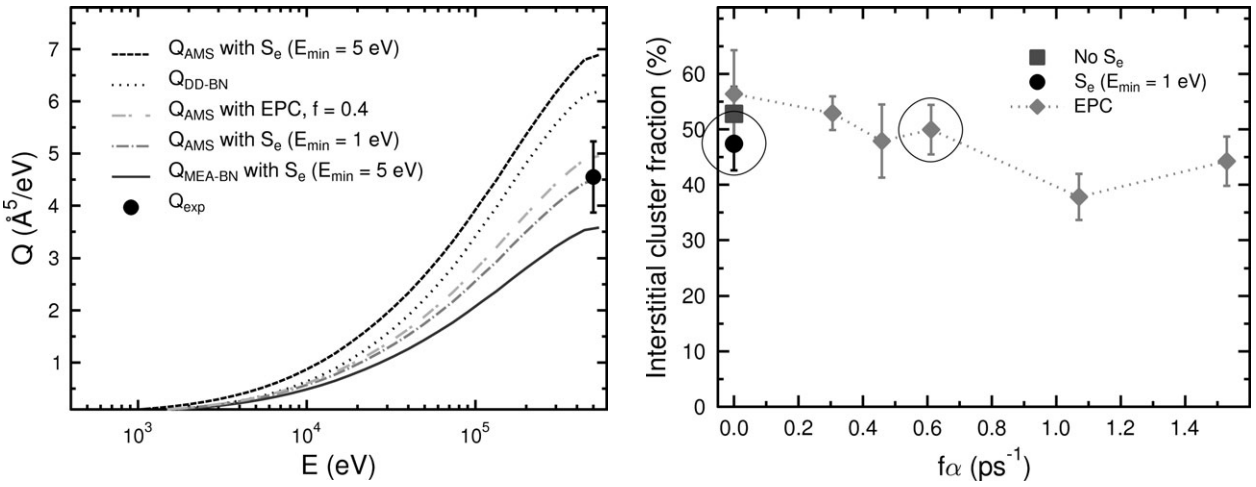

(a) (b)

Figure 10: (a) The cumulative simulated mixing efficiency Q as a function of primary recoil energy. The endpoint on the right side corresponds to the experimental irradiation energy. Data for the AMS and MEA-BN potentials with included electronic stopping S_e during the simulations, as well as DD-BN data with electronic stopping corrections (see Appendix of publication **IV**) are shown. In addition to this, AMS results with $S_e(E_{min} = 1$ eV) and with a scaled electron-phonon coupling strength (EPC) are shown. The experimental value is from Ref. [47] and the simulated data are from publication **IV**. (b) The fraction of vacancies in clusters after 20 keV cascades with different EPC coupling strengths and with different S_e criteria. In the case $f\alpha = 0$, no EPC is used and E_{min} in the S_e is 5 eV. The points corresponding to the conditions that lead to a correct mixing are encircled. From publication **IV**.

related to interactions with the plasma particles must be considered. These include activation and radiation damage caused by fusion neutrons.

In this section, the candidate structural materials are listed and the radiation damage they will experience is detailed. The challenges of modelling steels are also described.

4.1 Low-activation structural materials

Reducing the activation of a material is important, since the attraction of fusion as an energy source is based on its minimal environmental impact. This originates not only from the lack of exhaust gases but also from the fact that no long-term radioactive material is produced. Since T is one of the fusioning elements, some radioactivity is unavoidable, but careful design of reactor materials reduces the total amount considerably and the waste can be made innocuous in only 50-100 years [61].

Suitable low-activation elements have been shown to include C, silicon (Si), titanium (Ti), Fe, Cr and V, in addition to W in small amounts [62]. Minimizing the impurity content in a material is

also important. Based on this, candidates for structural materials are special, reduced activation ferritic/martensitic (RAFM) steels where Mo is replaced by W, V-Ti-Cr alloys and the ceramic silicon carbide (SiC) composites. Other inherent properties also make these materials desirable: RAFM steels with 9-12 % Cr contents have high resistance to swelling [63–65] and high thermal conductivity, V alloys have a high heat flux capability and exhibit low thermal expansion [61] and SiC has a high mechanical strength even at high temperatures.

4.2 Radiation damage

Only a small fraction of the energetic fusion neutrons will be absorbed in the first wall, which means that most of the 14 MeV energy is transferred into the blanket. Here it will produce radiation defects which can profoundly alter the properties of the blanket material, through either inelastic processes or elastic collisions [66]. The former processes include interactions with electrons or transmutations of (n,α) or (n,p), in which He or H (or rhenium in W) is formed. The amount of He and H that is produced in this way in a fusion reactor is expected to be about one order of magnitude higher than in fission reactors [66], causing swelling problems due to bubble formation and embrittlement due to He segregation at grain boundaries. For instance, the He production in Be when subject to an ITER relevant neutron fluence of 1 MWa/m^2 is 3500 atomic parts per million (appm) and in steels 150 appm [10].

A major concern is also the elastic collisions between the neutrons and target nuclei which result in cascades as described in Sec. 3.6. The resulting lattice damage consists of single defects, defect clusters, dislocation loops, precipitates and/or voids. The damage is often expressed in displacements per atom (dpa), which describes how often each atom in a material is on average displaced from its lattice site. Due to defect recombination as described in Sec. 3.6.1, the final displacements are often only a fraction of the initial dpa value. For a 1 MWa/m^2 neutron fluence, the damage in W is estimated to be 3.5 dpa [10].

As an example of irradiation induced defects, transmission electron microscope (TEM) images of damage produced in Fe due to Fe^{3+} ion bombardment are seen in Fig. 11. The white spots that are formed as the irradiation increases are interstitial loops, clearly showing that particle irradiation has a major impact on the microstructure of a material.

Since the mechanical and physical properties of a material are governed by its microstructure, it can undergo critical changes due to the lattice damage. For instance, the formation of defects into larger nanostructures together with precipitates effectively hinder the movement of dislocations, causing radiation induced embrittlement [67]. This includes hardening, loss of ductility, fracture toughness and

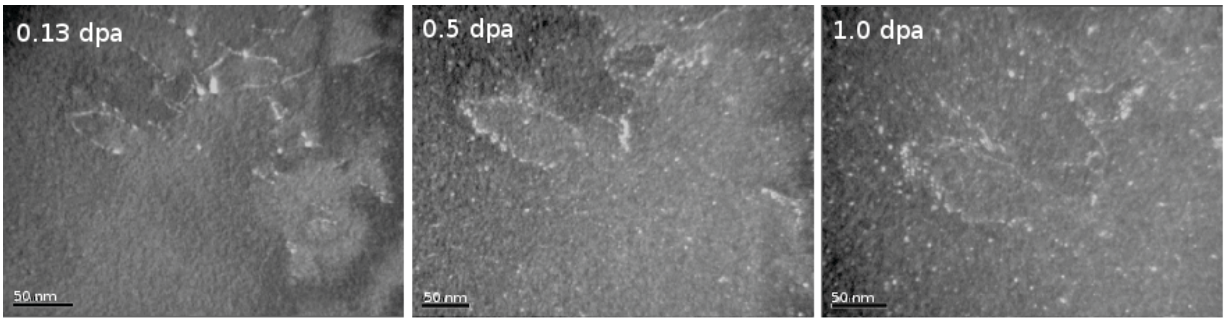

Figure 11: Interstitial loops and dislocations formed in iron during irradiation of 300 keV Fe^{3+} ions. Courtesy of Robin Shäublin, École Polytechnique Fédérale de Lausanne, Centre de Reserches en Physique des Plasmas, 2009.

creep strength. A shift in the ductile-to-brittle transition temperature (DBTT) of a material towards higher temperatures is also common.

Knowledge of the atom-level lattice defects is therefore vital in order to be able to predict the response to irradiation of structural materials and MD is often used for this reason, as done in publications **II** – **VI** in this thesis. The studied materials are V, W, WC, as well as Fe and FeCr.

4.3 Modelling of steels

The main constituent in RAFM steels is Fe, but they also contain significant concentrations of other elements. As an example, the steel alloy EUROFER 97 contains 9 at-% (atomic percent) Cr, 1 at-% W, and 0.48 at-% manganese (Mn) as well as V, tantalum (Ta) and C in small amounts [68]. The behaviour of steels under irradiation depends non-monotonically on the Cr content, for instance, a minimum in the DBTT shift is seen at a concentration of 9% Cr and the swelling exhibits a maximum at the same concentration [69]. Therefore, it is important to model not only pure Fe, but also Fe-Cr interactions correctly.

The work on Fe and FeCr in publications **II, IV** and **V** is part of an international effort, aiming at understanding the effect of Cr on the response of steels under irradiation, using a multi-scale approach [70–74]: information obtained from *ab initio* calculations of defect behaviour in FeCr (e.g. [33, 75–77]) is used as input when developing potentials to be used in MD [30, 31, 33, 45, 72], and further modelling is done by MC methods [73, 78]. Since the microscopic properties of FeCr alloys are coupled to their macroscopic behaviour, many attempts have been made to reproduce the defect energetics (ground state configurations, interactions with solute atoms and mobilities) and especially the solubility of Cr in Fe correctly [33, 70, 79]. An incorrect description of the latter results in an untruthful phase diagram [70, 78, 80].

The standard FeCr phase diagram as obtained using Thermo-calc and the Calphad database [81, 82] is illustrated in Fig. 12. Four different phases are visible: α, α′, σ and γ. Mixtures of these are also present at certain Cr concentrations and temperatures and the line separating the miscible region from that containing both Fe-rich (α) and Cr-rich regions (α′) is called *miscibility gap* [70, 78, 80].

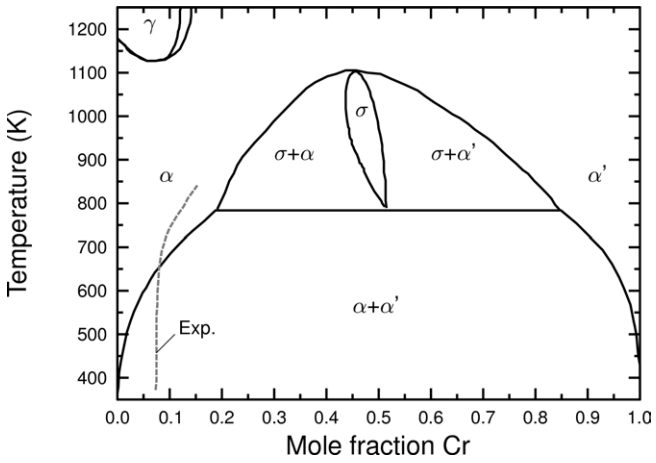

Figure 12: The standard FeCr phase diagram. The experimental curve is an average of data collected in Ref. [72].

Determining the short-range-order (SRO) parameter, which describes the local elemental ordering, is a way of getting knowledge of the phase, and consequently the solubility, at different concentrations [70, 78, 83]. For a given nth nearest neighbour cell, it is defined as

$$SRO = 1 - \frac{n_{BA}/n_B}{c_A}, \tag{25}$$

where n_{BA} is the number of neighbours of type A in the cell to atom type B, n_B the average number of neighbours to atoms of type B and c_A is the total concentration of A in the alloy. A positive value for the SRO parameter indicates that, on average, B atoms have more A neighbours than they would in a random solution. This means that the A atoms tend to be as far away from each other as possible, thereby producing a certain order in the alloy. A negative value, on the other hand, indicates that a clustering takes place and zero value implies a fully random distribution.

The SRO value in FeCr alloys has been determined experimentally, revealing that a change of sign occurs from negative to positive at a critical Cr concentration of about 10% at 703 K [83]. Also *ab initio* calculations have confirmed the existence of a critical concentration by calculating the heat of mixing of FeCr [33]. The underlying reason for this is the magnetic spins of the elements [84]. Taking the behaviour of the heat of mixing into account in the phase diagram, which was not done in the Calphad version, affects the slope of the low temperature miscibility gap by shifting it towards concentrations of about 9%. This is illustrated by the experimental line in Fig. 12.

The segregation behaviour of FeCr has an impact on its behaviour under irradiation, since the formation of α' phases (Cr precipitates) accelerates the embrittlement [72]. It is therefore desirable that the MD potentials that are used can reproduce the thermodynamics of FeCr alloys, particularly the heat of mixing. Two EAM-like FeCr potentials are, in fact, able to do this: one by separating the electron density and embedding functions into *s* and *d* electron contributions, hence denoted two-band model (2BM) [33], and the other by making the potential dependent on the local Cr concentration [85].

Whether or not the heat of mixing would induce phase separation at short time scales was tested in publication **V** by calculating the change in SRO in $Fe_{90}Cr_{10}$ due to cascades. This revealed no phase change (ΔSRO = 0) when a potential with correct heat of mixing was used (the 2BM) but a positive change, indicating Cr segregation, was seen when this was not the case. In a later study, where cascades in FeCr alloys of 5 and 15% Cr were performed with the 2BM potential [86], the change in SRO was negative for 5% and positive for 15%, as expected from the heat of mixing.

Other comparisons between different FeCr potentials in publication **V** revealed large differences in the Cr content in interstitial defects. Removing the contributions from the second band of the 2BM potential, thus creating a 1BM, only a small fraction of the interstitials contained Cr, whereas the fraction was around 10% for the 2BM. Another potential, CWP [32], predicted this fraction to be more than three times as high (see Fig. 13). The reason behind the 1BM behaviour is the negative interaction energy for a mixed FeCr <110> dumbbell when compared to a pure Fe-Fe one. This energy is positive within the 2BM, and also according to DFT calculations [70]. The high Cr content in CWP, on the other hand, is explained by the high mobility of a Fe interstitial in this potential. Here, an interstitial wrongly takes the <111> crowdion configuration and can thus glide in 1D, which makes it possible for the interstitial to find the closest Cr atom to form a mixed dumbbell even in the cascade time frame. The Fe mobility in the 2BM has a more complex nature, since the most stable interstitial configuration is the <110> dumbbell, which moves in a 3D manner and is therefore not as fast. The mobility activation energies are $\sim$0.03 eV and $\sim$0.3 for the CWP and AMS potential, respectively.

The simulations in publication **V** also resulted in a rather surprising conclusion, namely that the presence of Cr atoms does not significantly influence the primary damage in Fe when it comes to the total amount of defects and defect cluster fractions. This implies that the longer-term defect evolution, including diffusion and annihilation of defects, and not the initial defect distribution is associated with the observed Cr concentration dependency on properties of irradiated steels. For instance, the Cr effects on swelling in steels have been related to how Cr influences the migration of interstitial clusters [70].

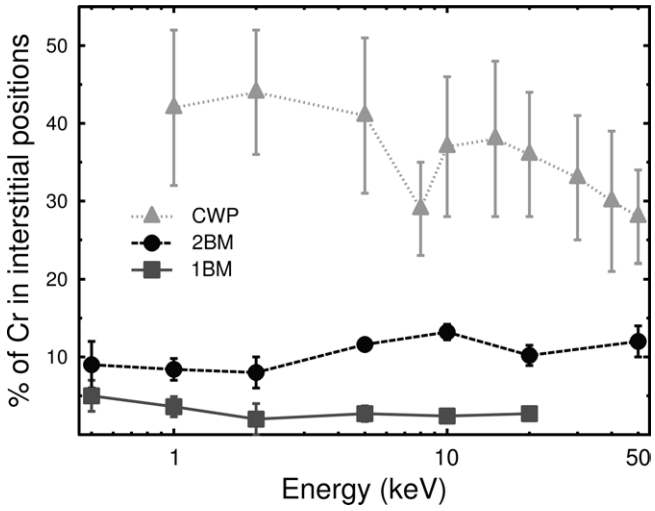

Figure 13: Cr fraction of all interstitial atoms as a function of recoil energy. Data obtained using three different potentials are illustrated.

Further progress in the modelling of steels includes the development of a FeC ABOP potential [87] and a magnetic Fe potential [31] (DD), which was modified and tested in **II** and **IV**. The effect of magnetism in DD is treated with an additional term in the embedding function, and its form is derived with the help of a combination of the Stoner and Ginzburg-Landau models [31].

5 DAMAGE IN PLASMA FACING MATERIALS

The plasma in the upcoming next-generation ITER device will differ greatly from that in any of the now-existing fusion devices, mainly due to ITER's goal to achieve an energy amplification factor of 10 during several hundred seconds pulses and a steady-state factor of 5 [88]. A single pulse will correspond to at least a year of operation in JET in terms of wall loads [3], highlighting the challenges that the wall materials are faced with. The main effects on the PFMs come from the constant bombardment of neutrons and other plasma particles, the high heat flux and the transient plasma disruptions. In this section, the key material responses to these issues, the changes in properties due to radiation damage, erosion, T retention and the formation of mixed materials will be described.

5.1 PFM lifetime issues

Since replacing the inner reactor parts is an intricate and expensive operation which needs remote handling as well as a reactor shut-down, the lifetime of the components must be maximized. This, in turn, means that the mechanical and physical properties of the PFMs must remain relatively stable

even after several thousands of plasma pulses. The materials that will face the plasma in ITER have been chosen to be Be for the main chamber wall, W for the divertor dome and baffle, and carbon fibre reinforced carbon (CFC) for the divertor strike points. The choice of Be and C is mainly based on the preference for low-Z materials, which, if eroded, do not cause as large radiation losses in the plasma as high-Z ones. Both C and W can operate at high temperatures without melting and W is additionally highly resistant against erosion.

Neutron bombardment crucially affects the bulk properties of the PFMs, since they are not magnetically confined and will escape the plasma, causing radiation damage in the materials as described in Sec. 4. The estimated neutron flux at the wall is 1-1.5$\times 10^{20}$ $\mathrm{m^{-2}s^{-1}}$, and the total neutron load at the wall and divertor in ITER is 0.3 MWa/$\mathrm{m^2}$ and 0.15 MWa/$\mathrm{m^2}$, respectively [8, 66]. In Be, this will result in erosion, swelling, a reduction in thermal conductivity and embrittlement. The thermal conductivity is also affected in C and in W, and a shift in the DBTT and swelling occurs [10].

Although the primary wall is supposed to be held out of contact with the plasma with the help of carefully designed magnetic field lines, repetitive bursts of the edge plasma (*edge localized modes*, ELMs) which transport heat to the walls and divertor will be expected. If operating in the high-confinement mode (H-mode), as planned in ITER, the ELMs are even needed, since depending on the type of ELM, 1-10% of the plasma energy and particles are removed, keeping the plasma density from increasing beyond the stability limit. Above this limit, plasma disruptions can occur, resulting in sudden energy fluxes to the reactor walls.

However, since the expected duration of type I ELMs in ITER is 0.2–1 ms with a frequency of 1–10 Hz [89] and the energy fluxes are in the range 0.5–5.0 MJ/$\mathrm{m^2}$ [88], the ELMs will substantially shorten the lifetime of the reactor components by evaporation. Mitigation of the ELMs can be achieved with noble gas puffing or by adding frozen fuel pellets, but this also reduces the confinement of the plasma [88].

5.2 Sputtering

Apart from the bulk changes, the surface of a PFM will undergo major changes in a reactor. Surface melting can occur, but erosion is highly critical: an estimated 3-10 mm of the low-Z materials Be and C and 0.03–0.3 mm of W will erode per year [8].

A surface is eroded by *sputtering*, which is simply the mechanism by which atoms are emitted from a surface due to particle bombardment [90]. There are three types of sputtering: physical, chemical and electronic. The latter type covers both sputtering due to electron irradiation and high ($\gtrsim$ 1 MeV)

energy ion bombardment where electronic excitations cause sputtering, and can be considerable in insulators. In this work, only physical and chemical sputtering are considered.

Physical sputtering occurs in the following way. Collision cascades are formed when the incoming ion enters the material, and the recoils can reach the surface atoms. An atom is then sputtered if it receives an energy directed normal to the surface that is comparable to the surface binding energy. Depending on the incoming particle energy, three regimes exist in this process: the single knock-on regime in which the energy is not sufficient to produce collision cascades, the linear cascade regime where a few cascades but not sub-cascades are created, and the spike regime, where the density of recoils is high and a heat spike is formed. Physical sputtering usually takes place for ions with energies above $\sim$10 eV.

If the bombarding particles form chemical bonds with the substrate, the sputtering can be either reduced, if for instance carbides or oxides are formed, or enhanced if gaseous molecules are formed. The chemical sputtering in, for example, C based materials is considerable [91] and sputtering has been observed for energies as low as 2 eV. The emittance of hydrocarbons from C materials under H isotope bombardment has been explained by a mechanism named *swift chemical sputtering* (SCS) [92, 93]. Here, an energetic particle penetrates between two C atoms, causing their bond to break, which releases a C surface atom together with any H isotope bound to it. The momentum transfer to the carbon atoms involved in the process depends on the time that the incoming H isotope spends between them, which means that a high energy as well as a low energy limit for this process exist.

The sputtering yield Y is defined as the number of outgoing atoms per incoming particle. This quantity can be measured with different experimental techniques, such as weight-loss methods, spectroscopy, or with the help of field-ion microscopes [90]. Binary-collision approximation-based codes such as TRIM [94] are an efficient way to study the physical sputtering, but MD must be used for studying chemical sputtering where low-energy many-body interactions are important.

5.2.1 Chemical sputtering of beryllium

In publications **I** and **VII**, the sputtering of Be due to self-ion and D bombardment in a fusion relevant energy range 3 – 100 eV was simulated, using the potentials developed in **I**. Fig 14 shows the simulation setup. The starting point for the bombarding ion was set to 5 Å above the surface of the simulation cell, which contained 3388 atoms. The temperature at the borders and the bottom was controlled to room temperature during the first 2 ps of the simulation in order to mimic an infinite lattice, and the temperature of the whole cell was controlled during the rest of the 7 ps run. The two bottom-most layers were fixed during the whole run. After one bombardment, the final cell was used

as input in the next simulation to model cumulative bombardment. Between two runs, the cell was shifted randomly in x and y directions, so that the surface was evenly irradiated although the ion was always directed to the middle of the cell. The direction of the ions was normal to the surface.

Two different surface terminations were considered: (0001) and $(\overline{1}\overline{1}20)$. In the D bombardment simulations, 'rough' versions of these were additionally used. Rough surfaces resemble a real situation where the surface has been subject to prolonged bombardment. These were constructed by randomly removing about half of the Be atoms in the first layer of the respective surface.

The sputtering yield and minimum ion energy needed for sputtering, *i.e.* the threshold energy, in Be self-bombardment was seen to agree well with experimental values, working as a benchmark for the potential. During the bombardment simulations, amorphous regions were formed in the bulk, but the structure recrystallized through collective migration of the defects to the surface. The adatoms created in this way contributed to the surface growth.

An interesting chemical effect was observed in the D bombardment simulations, namely that most of the sputtered Be atoms at low energies were released as part of a BeD molecule. This is illustrated

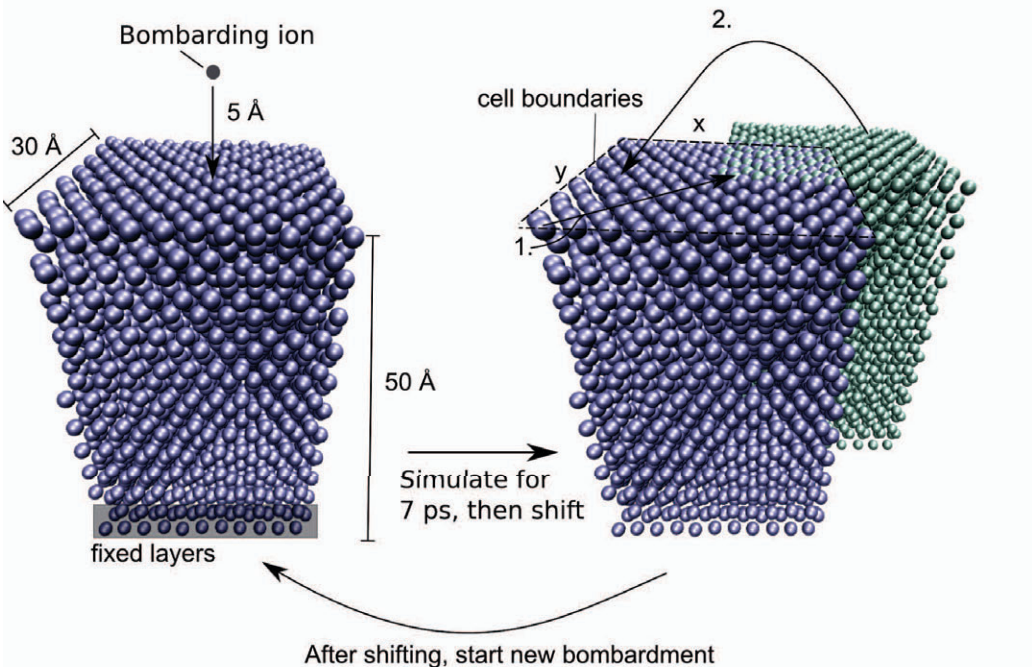

Figure 14: The setup in the cumulative sputtering simulations. The starting point for the energetic ion is 5 Å above the surface, and it is directed normal to the surface. Cells of 3388 atoms are used and the dimensions are as shown. The two bottom-most atom layers are fixed. To ensure an even bombardment of the surface, the atoms are shifted randomly in x and y directions (arrow 1) after which periodic boundaries are enforced (arrow 2). This is done after each bombardment and the shifted cell is then used for the next simulation, so that the bombardment is cumulative.

in Fig. 15, where the fraction of Be that is sputtered as BeD molecules is plotted as a function of incoming D energy. The fraction is $\sim$100% at 7–20 eV and decreases with increasing ion energy.

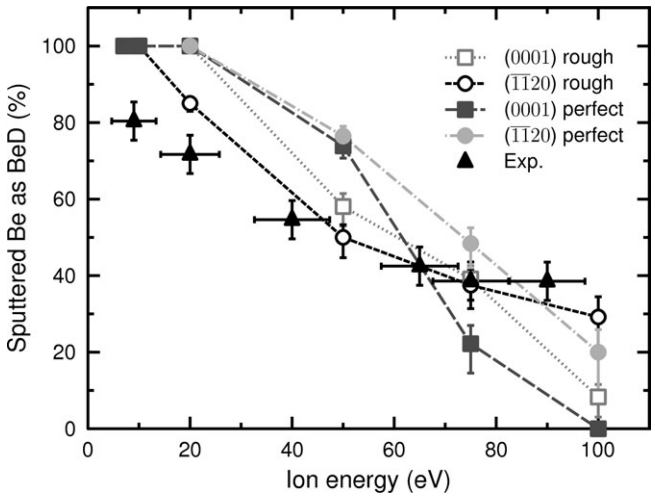

Figure 15: The fraction of Be atoms sputtered as BeD molecules after Be exposure to a D plasma. Both simulated and experimental data are shown. Two different orientations of the Be surface and both initially rough and perfect surfaces were used in the simulations. From publication **VII**.

BeD molecule sputtering has also been observed in JET [95] and in the linear divertor plasma simulator PISCES-B facility in San Diego [96, 97]. Additional experiments were performed in PISCES-B in order to investigate the ion energy dependency on the BeD molecule sputtering as revealed by the simulations (see Fig. 15). Be targets were exposed to a D plasma, and sputtered BeD molecules were measured in front of the target. The energy of the incident D ions was controlled by negatively biasing the target with respect to the plasma potential and BeD molecules were identified by observing the band emission spectrum. The surface temperature was $\sim$400 K and the flux was $3{\cdot}10^{22}\mathrm{m}^{-2}\mathrm{s}^{-1}$.

The experimentally observed fraction of Be released as BeD is added to the simulation data in Fig. 15. The same ion energy dependency is seen and a clear chemical effect is therefore present also in the experiments. In an earlier similar experiment, the BeD molecules were observed to be released with much higher energies than the energy characterized by the surface temperature, implying that the underlying mechanism is not chemical erosion, but rather chemical sputtering [96]. This was confirmed in the simulations, where the sputtering mechanism, more precisely, was identified as SCS.

This finding proves the previous notion that SCS is important only in covalently bonded materials (such as C, Si) wrong [93]. The basis for the notion is the fact that in covalent materials, loosely bound chains can easily be formed at the surface, but in close-packed metals like Be, even the surface atoms have a large number of bonds, hence, the breaking of one of these does not affect the surface binding essentially. However, if the surface is damaged and a Be atom has many H isotopes bound to it, its binding to the surface is weak and it can therefore be sputtered even at low energies.

The SCS mechanism in Be is illustrated in Fig. 16. Here, a 10 eV D ion is bombarding a Be surface, resulting in sputtering of a BeD and a D_2 molecule. The graph illustrates both the potential energy of all Be atoms initially within the potential cutoff (2.9 Å) to the sputtered Be atom and the kinetic energy of the incoming D ion. In the upper part of the figure, the sputtering process is illustrated with snapshots of the situation at six different times, labelled a-f. The corresponding times are indicated with vertical lines in the energy graph. The D ion is seen to enter between three Be pairs, consequently breaking three of the initial five Be bonds the soon-to-be-sputtered Be atom has.

The ion energy dependency of the fraction of Be released as BeD molecules can be explained by the fact that the number of D neighbours to Be surface atoms decreases with increasing D ion energy. This, in turn, is due to the deeper penetration at high energies. Since a high amount of D neighbours makes the Be atoms weakly bonded to the surface, and a D neighbour often sputters with any released Be atom, the fraction is naturally higher at low energies. The average amount of initial D neighbours of sputtered Be atoms was seen to be as high as 3 for ion energies of 7–10 eV. The Be neighbours increased from about 5 to ideal 9 in the 7–100 eV energy range.

5.3 Dust

Most of the eroded material will redeposit somewhere in the reactor. If deposited on cool surfaces, the material could form layers that are only weakly adhered to the surface and therefore easily released during transient events (*e.g.* arcing, ELMs). This creates *dust* particles, *i.e.* agglomerates of particles in the 1–100 μm range [98], which are often composed of mixed materials.

Since this dust might be tritiated, radioactive and/or toxic, a safety limit for ITER has been set to 10 kg for 10 μm particles and 100 kg for 100 μm ones [99]. Even smaller inventories are allowed for hot surfaces like the divertor. Other dust-related problems are deposits on optical diagnostics and the possibility of reactions with coolants or air in the event of leaks. Steam reactions produce H in significant amounts, which could lead to combustion if mixed with air, and a vacuum leak could result in carbon dust explosion, *i.e.* rapid dust oxidation.

5.4 Tritium retention

Trapping of the radioactive T is a critical issue from a radiological viewpoint, and a limit of 700 g T for ITER has been set [100]. T can migrate deep inside the walls and be trapped at remote locations, making removal difficult. In addition, it readily forms compounds with C and will hence bind to re-deposited C. Since eroded C migrates in the chamber, the actual location of the T sources is difficult

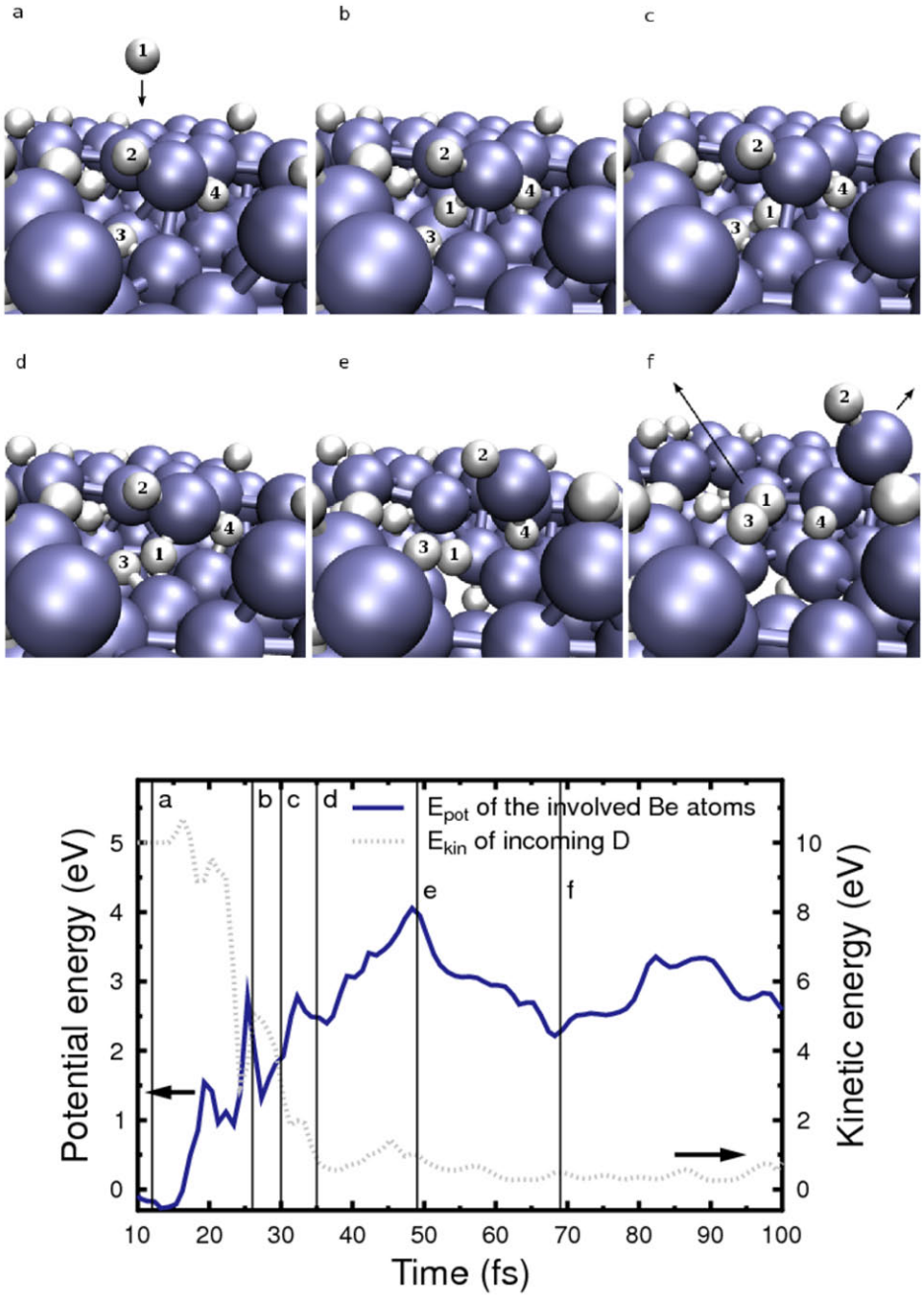

Figure 16: An illustration of a sputtering event in Be due to D bombardment. In the upper part of the figure, snapshots of the situation at six different times during the process are seen. The D atoms are represented by small light grey spheres and the Be atoms are the larger blue spheres. The graph in the lower part illustrates the kinetic energy of the incoming 10 eV D ion (dotted line) and the potential energy of the Be atoms that are initially bonded with the sputtered Be atom (solid line). The initial potential energy of these is chosen as zero level energy. The times corresponding to the snapshots are indicated with vertical lines in the graph and the arrows in the last snapshot (f) show in which direction the sputtered D_2 and BeD molecules are moving. From publication **VII**.

to predict, but ^{13}C puffing experiments indicate that most of the C goes to the inner divertor [101]. Radiation defects increase the T retention, since dislocation loops, voids and grain boundaries effectively work as traps. Annealing of the defects helps remove the T, and indeed, neutron irradiation experiments on CFCs have shown a reduction in the retention at higher temperatures [10].

Although not as critical as in C based materials, the retention in Be must also be considered. The main source of T here are the transmutation processes due to neutron irradiation, but T is also codeposited with eroded Be. The expected inventory (depending on the trap concentration) will be of the order 20 g after 12000 pulses and irradiated Be has been shown to trap more T than an unirradiated specimen [10]. Be releases T when kept at temperatures above $\sim$600°, but since the walls in ITER will be kept at $\sim$300°, essentially all T will remain trapped if not released with eroded Be. *Bake-outs*, *i.e.* several-day long periods when the vessel is held at high temperatures, possibly in an oxygen atmosphere, are a possible means of removing impurities and T.

5.5 Formation of mixed materials

Sputtering, transformation and redeposition will result in formation of mixed materials at the reactor surfaces. The properties of these materials can differ strongly from those of their constituents, e.g. a mix of Be and W (in the form of Be_2W, $Be_{12}W$ or $Be_{22}W$) will melt at temperatures well below the W melting point, posing severe melting problems. The formation on Be layers on C-based materials (as Be_2C) will have a mitigating effect on both the sputtering and T retention [102, 103].

Mixed WC alloys have been studied extensively (see *e.g.* [104] and references therein), and for instance, the hydrogen isotope retention levels were found to lie between that of pure C and W. MD methods have also been used to model sputtering in WC [105] and radiation damage in the system was studied by simulating cascades in publication **VI**. The simulations revealed that WC exhibits a defect recombination similar to that in metals: only about 10% of the maximum number of defects remained at the end of the cascades. Moreover, a major part of the single defects that are formed was C defects, which could have an influence on long term defect evolution, since single defects easily migrate to grain boundaries or surfaces.

This is illustrated in Fig. 17, where the average of both the total amount of defects and isolated ones after W recoil cascades are plotted as a function of recoil energy. As the energy increases, the total amount of defects as well as isolated C defects increases, whereas the opposite is true for isolated W defects.

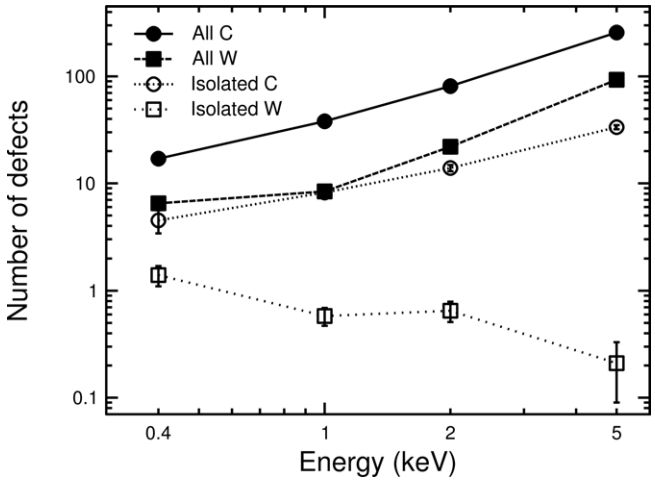

Figure 17: The average total and isolated defects after collision cascades induced by W recoils in WC. From publication **VI**.

Purely ballistic effects that would be associated with the mass difference between W and C could not explain the phenomena, since TRIM simulations did not agree with the MD ones. Also, the defect thresholds were shown to be similar for both elements. However, at an early stage of the cascade, the defects displayed no elemental asymmetry, indicating that recombination effects are important. Indeed, since the formation energy for creating a W interstitial and a vacancy is 12 and 3 eV, respectively, it is energetically highly favourable for W defects to recombine. The corresponding C energies are 2.7 and 0.5 eV, which explain why C defects do not recombine at the same rate. The recoil energy dependency is explained by the fact that larger heat spikes are formed at higher energies, enabling more recombination.

5.6 Materials in reactors beyond ITER

The ITER machine is designed as a test reactor and to prove that fusion as an energy source is not mere science fiction. The reactors following ITER, on the other hand, will be large scale power plants, continuosly producing substantial amounts of electricity. For instance, when finished, the future Demonstration Power Reactor (DEMO) will have an output energy of 2–4 GW, resulting in even more harsh conditions for the plasma facing materials: the wall load is estimated to be 2–3 MW/m^2 and the neutron fluence at the first wall will result in about 30–80 dpa per year [106]. At such conditions, the erosion rate and tritium retention in Be and C will be unacceptably large and an all-W reactor is the most probable solution [10]. Also, depending on the retention during the first phase in ITER where only D fuel is used, the C parts of the reactor might be replaced with W ones before any T is added.

6 CONCLUSIONS

In this thesis, analytical bond-order interatomic potentials for molecular dynamics (MD) simulations were developed for Be-Be, Be-C and Be-H systems. These were shown to be able to describe not only bulk and defect properties, but also the Be self-sputtering process and the formation of Be_2C layers during C bombardment of Be. The developed potentials can be used to study plasma-surface interaction in fusion reactors, such as neutron radiation damage, formation of mixed materials, T retention and sputtering processes.

Sputtering of Be when exposed to a D plasma was simulated using the Be-H potential. The results showed that a large fraction of Be is released as BeD molecules at low (7-20 eV) D ion energies, and that this fraction decreases with increasing ion energy. This trend was also observed in experiments, confirming that chemical sputtering is important in Be. The underlying mechanism for the sputtering was identified as being the swift-chemical sputtering process, previously believed to be important only in covalent materials.

Since Fe is the main component of ferritic/martensitic steels which are currently considered as structural material for future fusion reactors, a correct modelling of radiation damage in Fe is vital. The short range part of two Fe potentials was therefore modified in order to be better suited for collision cascade processes. Upon the modifications, the potentials were able to reproduce the experimental defect thresholds in Fe and the previously large scatter between potentials concerning the description of primary defects was reduced.

The influence of electronic effects on primary damage was studied by comparing simulated and experimental values of the ion-beam mixing efficiency. The mixing was seen to depend on the melting properties of the Fe potentials; a high melting point resulted in a low mixing. Using a potential with a reasonable melting point resulted in agreement with experiments only if electronic stopping (S_e) was applied for atoms with an energy above 1 eV or if a combination of electron-phonon coupling (EPC) and S_e was used. In the latter case, EPC with a time constant of 1.6352 ps was included for atoms with energies below the cohesive energy of Fe, and S_e was used elsewhere. EPC was seen to affect the primary damage mostly in terms of an increasing amount of total defects, by removing heat from the hot cascade core and thus shortening the heat spike and making recombination harder. The same effects were observed for the S_e.

The behaviour of steels under irradiation has been observed to depend strongly on the Cr content. Here, the effect of Cr on primary damage in the $Fe_{90}Cr_{10}$ alloy was investigated, revealing that Cr has no influence on the defect clustering nor on the total amount of defects that are created. However, depending on the potentials that were used in the simulations, an accumulation of Cr in interstitial

defects was seen. Defect evolution on a longer time-scale was concluded to be responsible for the Cr influence on the irradiation behaviour.

Whether or not cascades induce phase separations in FeCr was also investigated by calculating the change in the short range order. When using a FeCr potential with a correct description of the heat of mixing, no phase separation was seen.

V alloys are also candidate materials for reactor structures and the primary damage in V as well as in the divertor material W was studied. Prior to the cascade simulations, the potentials used were first tuned to reproduce the defect thresholds. When comparing the damage in the two different elements with that in Fe, several properties affecting the outcome of a cascade were identified. These are the melting point, the defect formation energy and mobility, and subcascade threshold.

When studying the radiation damage in the mixed WC alloy, it was seen that most of the damage was in the form of empty C lattice sites or C interstitial atoms. This was ascribed to the high defect formation energies in W, which makes it energetically favourable for W defects to recombine. Single C defects are highly mobile and surfaces and grain boundaries can therefore be segregated by C under irradiation of WC.

To conclude, the analyses, models and techniques in this thesis have improved the reliability of irradiation simulations as well as our possibilities to model complicated systems containing several different species. The thesis has also given more insight into both plasma-wall interactions and primary damage in fusion reactor materials. Hence, it will contribute to prolonging the operational life time, and by that increasing the benefits, of future fusion reactors.

ACKNOWLEDGMENTS

I wish to thank the head of the laboratory, Prof. Jyrki Räisänen, for providing the facilities of the laboratory to my disposal. I also thank Prof. Juhani Keinonen, the head of the Department of Physics, for the opportunity to conduct research at the department.

Many thanks are due to my supervisor, the ever optimistic Prof. Kai Nordlund. Although eminently busy, he has always found the time to answer my questions and to guide me further.

The many years at the Accelerator Laboratory have been enjoyable mostly thanks to my co-workers and equally friends. Special thanks go to my long-term room mates Toffe, Nicke and Jani, and also to Tommi and Eero who have kept my working tool alive and almost bug-free. I have also really enjoyed all the non-scientific times we have spent together.

Most of all, I would like to thank Miku, without whom neither my research nor my life would seem meaningful. I also appreciate the warm support that my family has given me.

Financial support from the National Graduate School in Materials Physics, Magnus Erhnrooth's Foundation and Väisälä Foundation is gratefully acknowledged.

Helsinki, August 28, 2009
Carolina Björkas

References

1. *BP Statistical Review of World Energy 2009*, available at *http://www.bp.com*.

2. *IPCC Fourth Assessment Report*, available at *http://www.ipcc.ch/ipccreports/ar4-wg1.htm*.

3. A. W. Kleyn, N. J. Lopez Cardazo, and U. Samm, *Plasma-surcace interaction in the context of ITER*, Physical Chemistry Chemical Physics **8**, 1761 (2006).

4. European Fusion Development Agreement, *http://www.efda.org*.

5. The Joint European Torus, *http://www.jet.efda.org*.

6. W. J. Nuttall, *Fusion as an Energy Source: Challenges and Opportunities*, Institute of Physics: Report (2008).

7. ITER Physics Basis Editors and ITER Physics Expert Group Chairs and Co-Chairs and ITER Joint Central Team and Physics Integration Unit, *ITER Physics basis*, Nuclear Fusion **39**, 2137 (1999).

8. H. Bolt, V. Barabash, G. Federici, J. Linke, A. Loarte, J. Roth, and K. Sato, *Plasma facing and high heat flux materials - needs for ITER and beyond*, Journal of Nuclear Materials **307-311**, 43 (2002).

9. D. K. Morozov, E. O. Baranova, and I. Y. Senichenkov, *Impurity Radiation from a Tokamak Plasma*, Plasma Physics Report **22**, 906 (2007).

10. V. Barabash, G. Federici, J. Linke, and C. H. Wu, *Material/plasma surface interaction issues following neutron damage*, Journal of Nuclear Materials **313-316**, 42 (2003).

11. D. J. Ward and S. L. Dudarev, *Economically competitive fusion*, Materials Today **11**, 46 (2008).

12. P. Vladimirov and A. Möslang, *Comparison of material irradiation conditions for fusion, spallation, stripping and fission neutron sources*, Journal of Nuclear Materials **329-333**, 233 (2004).

13. B. J. Alder and T. E. Wainwright, *Studies in Molecular Dynamics. I. General Method*, J. of Chem. Phys. **31**, 459 (1959).

14. D. C. Rapaport, *The Art of Molecular Dynamics Simulation*, 2nd ed. (Cambridge University Press, United Kingdom, 2004).

15. M. P. Allen and D. J. Tildesley, *Computer Simulation of Liquids* (Oxford University Press, Oxford, England, 1989).

16. K. Nordlund, 2006, PARCAS computer code. The main principles of the molecular dynamics algorithms are presented in [107, 108]. The adaptive time step and electronic stopping algorithms are the same as in [109].

17. M. S. Daw and M. I. Baskes, *Embedded-atom method: Derivation and application to impurities, surfaces, and other defects in metals*, Physical Review B **29**, 6443 (1984).

18. J. Tersoff, *New Empirical approach for the structure and energy of covalent systems*, Phys. Rev. B **37**, 6991 (1988).

19. K. Albe, K. Nordlund, and R. S. Averback, *Modeling metal-semiconductor interaction: Analytical bond-order potential for platinum-carbon*, Phys. Rev. B **65**, 195124 (2002).

20. H. J. C. Berendsen, J. P. M. Postma, W. F. van Gunsteren, A. DiNola, and J. R. Haak, *Molecular dynamics with coupling to external bath*, J. Chem. Phys. **81**, 3684 (1984).

21. K. Nordlund and S. L. Dudarev, *Interatomic potentials for simulating radiation damage effects in metals*, Comptes Rendus Physique **9**, 343 (2008).

22. M. Müller, P. Erhart, and K. Albe, *Analytic bond-order potential for bcc and fcc iron - comparison with established EAM potentials*, J. Phys.: Condens. Matter **19**, 326220 (2007).

23. G. C. Abell, *Empirical chemical pseudopotential theory of molecular and metallic bonding*, Phys. Rev. B **31**, 6148 (1985).

24. L. Pauling, *The nature of the chemical bond*, 3rd ed. (Cornell University Press, Ithaca, 1960).

25. F. Cleri and V. Rosato, *Tight-binding potentials for transition metals and alloys*, Phys. Rev. B **48**, 22 (1993).

26. D. W. Brenner, *Empirical potential for hydrocarbons for use in simulating the chemical vapor deposition of diamond films*, Phys. Rev. B. **42**, 9458 (1990).

27. K. Albe, J. Nord, and K. Nordlund, *Dynamic charge-transfer bond-order potential for gallium nitride*, Phil. Mag. A (2009), accepted for publication.

28. N. W. Ashcroft and N. D. Mermin, *Solid State Physics* (Saunders College, Philadelphia, 1976).

29. M. W. Finnis and J. E. Sinclair, *A simple empirical N-body potential for transition metals*, Phil. Mag. A **50**, 45 (1984), *see also Erratum, ibid. 53 (1986) 161*.

30. G. J. Ackland, M. I. Mendelev, D. J. Srolovitz, S. Han, and A. V. Barashev, *Development of an interatomic potential for phosphorus impurities in alpha -iron*, J. Physics: Condensed Matter **16**, S2629 (2004).

31. S. L. Dudarev and P. M. Derlet, *A magnetic interatomic potential for molecular dynamics simulations*, J. Phys.: Condens. Matter **17**, 1 (2005).

32. R. Chakarova, V. Pontikis, and J. Wallenius, *Development of Fe(bcc)Cr many body potential and cohesion model*, Delivery Report WP6, SPIRE project, EC contract no. FIKW-CT-2000-00058 (2002), http://www.neutron.kth.se/publications.

33. P. Olsson, J. Wallenius, C. Domain, K. Nordlund, and L. Malerba, *Two-band modeling of* α*-prime phase formation in Fe-Cr.*, Phys. Rev. B **72**, 214119 (2005).

34. P. M. Derlet, D. Nguyen-Manh, and S. L. Dudarev, *Multiscale modeling of crowdion and vacancy defects in body-centered-cubic transition metals*, Phys. Rev. B **76**, 054107 (2007).

35. J. F. Ziegler, J. P. Biersack, and U. Littmark, *The Stopping and Range of Ions in Matter* (Pergamon, New York, 1985).

36. F. Maury, M. Biget, P. Vajda, A. Lucasson, and P. Lucasson, *Frenkel Pair Creation and Stage I Recovery in W Crystals Irradiated Near Threshold*, Radiation Effects **38**, 53 (1978).

37. H. Neely, D. W. Keefer, and A. Sosin, *Electron irradiation and recovery of tungsten*, Physica Status Solidi **28**, 675 (1968).

38. J. A. DiCarlo and J. T. Stanley, *Energy dependence of electron-induced radiation damage in tungsten*, Nasa Report TN D-6464 (1971).

39. E. A. Kenik and T. E. Mitchell, *Orientation dependence of the threshold displacement energy in copper and vanadium*, Philosophical Magazine **32**, 815 (1975).

40. M. G. Miller and R. L. Chaplin, *Defect production in vanadium by low energy electron irradiations*, Radiation Effects and Defects in Solids **22**, 99 (1974).

41. P. Jung and G. Lucki, *Damage production by fast electrons in dilute alloys of vanadium, niobium and molybdenum*, Radiation Effects and Defects in Solids **26**, 99 (1975).

42. T. Diaz de la Rubia, R. S. Averback, R. Benedek, and W. E. King, *Role of Thermal Spikes in Energetic Collision Cascades*, Phys. Rev. Lett. **59**, 1930 (1987), erratum: Phys. Rev. Lett. 60 (1988) 76.

43. D. J. Bacon, A. F. Calder, and F. Gao, *Computer Simulation of Displacement Cascade Effects in Metals*, Rad. Eff. Def. in Sol. **141**, 283 (1997).

44. L. Malerba, *Molecular dynamics simulation of displacement cascades in α-Fe: A critical review*, Journal of Nuclear Materials **351**, 28 (2006).

45. D. Terentyev, C. Lagerstedt, P. Olsson, K. Nordlund, J. Wallenius, and L. Malerba, *Effect of the interatomic potential on the features of displacement cascades in α-Fe: a molecular dynamics study*, J. Nucl. Mater. **351**, 65 (2006).

46. C.-C. Fu, F. Willaime, and P. Ordejón, *Stability and Mobility of Mono- and Di-Interstitials in α-Fe*, Phys. Rev. Lett **92**, 175503 (2004).

47. S.-J. Kim, M.-A. Nicolet, R. S. Averback, and D. Peak, *Low-temperature ion-beam mixing in metals*, Phys. Rev. B **37**, 38 (1988).

48. M. W. Finnis, P. Agnew, and A. J. E. Foreman, *Thermal excitation of electrons in energetic displacement cascades*, Phys. Rev. B **44**, 44 (1991).

49. I. Koponen, *Atomic mixing in ion-bombardment-induced temperature spikes in metals*, J. Appl. Phys. **72**, 1194 (1992).

50. Q. Hou, M. Hou, L. Bardotti, B. Prével, P. Mélinon, and A. Perez, *Deposition of AuN clusters on Au(111) surfaces. I. Atomic-scale modeling*, Phys. Rev. B **62**, 2825 (2000).

51. J. le Page, D. R. Mason, C. P. Race, and W. M. C. Foulkes, *How good is damped molecular dynamics as a method to simulate radiation damage in metals?*, New J. Phys. **11**, 013004 (2009).

52. I. Koponen, *Energy transfer between electrons and ions in dense displacement cascades*, Phys. Rev. B **47**, 14011 (1993).

53. W. G. Kapinos and D. J. Bacon, *Effect of melting and electron-phonon coupling on the collapse of depleted zones in copper, nickel and* α*-iron*, Phys. Rev. B **53**, 8287 (1996).

54. D. M. Duffy and A. M. Rutherford, *Including the effects of electronic stopping and electron-ion interactions in radiation damage simulations*, J. Phys. Cond. Matter **19**, 016207 (2007).

55. M. Spaczér, A. Almazouzi, R. Schäublin, and M. Victoria, *Cascade overlap induced amorphization and disordering in irradiated intermetallics NiAl and* Ni_3Al*: a molecular dynamics study*, Rad. Eff. & Def. in Sol. **141**, 349 (1997).

56. A. J. E. Foreman, W. J. Phythian, and C. A. English, *Molecular Dynamics simulation of irradiation damage cascades in copper using a many-body potential*, Rad. Eff. & Def. in Sol. **129**, 25 (1994).

57. A. Caro and M. Victoria, *Ion-electron interaction in molecular-dynamics cascades*, Phys. Rev. A (General Physics) **40**, 2287 (1989).

58. A. Rutherford and D. Duffy, *The effect of electron-ion interactions on radiation damage simulations*, Journal of Physics: Condens. Matter **19**, 496201 (2007).

59. S. Khakshouri and D. M. Duffy, *Influence of electronic effects on the surface erosion of tungsten*, Physics Review B **80**, 035415 (2009).

60. K. Nordlund, L. Wei, Y. Zhong, and R. S. Averback, *Role of electron-phonon coupling on collision cascade development in Ni, Pd and Pt*, Phys. Rev. B (Rapid Comm.) **57**, 13965 (1998).

61. E. Bloom, *The challenge of developing structural materials for fusion power systems*, Journal of Nuclear Materials **258-263**, 7 (1998).

62. M. Victoria, N. Baluc and P. Spätig, *Structural Materials for Fusion Reactors*, available at http://www.iaea.org/programmes/ripc/physics/fec2000/html/node312.htm.

63. A. Kohyama, A. Hishinuma, D. Gelles, R. Klueh, and K. Ehrlich, *Low-activation ferritic and martensic steels for fusion application*, Journal of Nuclear Materials **233-237**, 138 (1996).

64. S. I. Porollo, A. M. Dvoriashin, A. N. Vorobyev, and Y. V. Konobeev, *The microstructure and tensile properties of Fe-Cr alloys after neutron irradiation at 400°C to 5.5 – 7.1 dpa*, Journal of Nuclear Materials **256**, 247 (1998).

65. B. Sencer and F. Garner, *Compositional and temperature dependence of void swelling in model Fe-Cr base alloys irradiated in the EBR-II fast reactor*, Journal of Nuclear Materials **283-287**, 164 (2000).

66. N. Baluc, *Materials for fusion power reactors*, Plasma Phys. Control. Fusion **48**, B165 (2006).

67. G. R. Odette and G. E. Lucas, *Embrittlement of Nuclear Reactor Pressure Vessels*, JOM **53**, 18 (2001).

68. G. A. Cottrell, S. L. Dudarev, and R. A. Forrest, *Immobilization of interstitial loops by substitutional alloy and transmutation atoms in irradiated metals*, Journal of Nuclear Materials **325**, 195 (2003).

69. F. Garner, M. Toloczko, and H. Sencer, *Comparison of swelling and irradiation creep behavior of fcc-austenitic and bcc-ferritic/martensitic alloys at high neutron exposure*, Journal of Nuclear Materials **276**, 123 (2000).

70. L. Malerba, D. Terentyev, G. Bonny, A. V. Barashev, C. Björkas, N. Juslin, K. Nordlund, C. Domain, P. Olsson, R. Chakarova, N. Sandberg, and J. Wallenius, *Modelling of radiation damage in Fe-Cr alloys*, J. ASTM **11**, JAI100692 (2007), proceedings of the ASTM 23rd Symposium on Effects of Radiation on Materials.

71. L. Malerba, A. Caro, and J. Wallenius, *Multiscale modelling of radiation damage and phase transformations: The challenge of FeCr alloys*, J. Nucl. Mater. **382**, 112 (2008).

72. L. Malerba, M. C. Marinica, N. Anento, C. Björkas, H. Nguyen, C. Domain, F. Djurabekova, P. Olsson, K. Nordlund, A. Serra, D. Terentyev, F. Willaime, and C. Becquart, *Comparison of empirical interatomic potentials for iron applied to radiation damage studies*, J. Nucl. Mater. (2009), submitted for publication.

73. C. Fu, J. Dalla Torre, F. Williame, J.-L. Bocquet, and A. Barbu, *Multiscale modelling of defect kinetics in irradiated iron*, Nature Materials **4**, 68 (2005).

74. A. Souidi, C. Bequart, C. Domain, D. Terentyev, L. Malerba, A. Calder, D. Bacon, R. Stoller, Y. N. Osetsky, and M. Hou, *Dependence of radiation damage accumulation in iron on underlying models of displacement cascades and subsequent defect migration*, Journal of Nuclear Materials **355**, 89 (2006).

75. P. Olsson, *Modelling of Formation and Evolution of Defects and Precipitates in Fe-Cr Alloys of Reactor Relevance*, Ph.D. thesis, Uppsala University, 2005.

76. T. P. C. Klaver, P. Olsson, and M. W. Finnis, *Interstitials in FeCr alloys studied by density functional theory*, Phys. Rev. B **76**, 214110 (2007).

77. C.-C. Fu, F. Willaime, and P. Ordejón, *Stability and Mobility of Mono- and Di-Interstitials in α-Fe*, Phys. Rev. Lett. **92**, 175503 (2004).

78. P. Erhart, A. Caro, M. Serrano de Caro, and B. Sadigh, *Short-range order and precipitation in Fe-rich Fe-Cr alloys: Atomistic off-lattice Monte Carlo simulations*, Physical Review B **77**, 134206 (2008).

79. S. Dudarev, J.-L. Boutard, R. Lässer, M. Caturla, P. Derlet, M. Fivel, C.-C. Fu, M. Lavrentiev, L. Malerba, M. Mrovec, D. Nguyen-Manh, K. Nordlund, M. Perlado, R. Schäublin, H. V. Swygenhoven, D. Terentyev, J. Wallenius, D. Weygand, and F. Willaime, *The EU programme for modelling radiation effects in fusion reactor materials: An overview of recent advances and future goals*, Journal of Nuclear Materials **386-388**, 1 (2009).

80. G. Bonny, D. Terentyev, and L. Malerba, *On the α–α' miscibility gap of Fe-Cr alloys*, Scripta Materiala **59**, 1193 (2008).

81. *http://www.thermocalc.com*.

82. *http://www.calphad.com/iron-chromium.html*.

83. I. Mirebeau, M. Hennion, and G. Parette, *First Measurement of Short-Range-Order Inversion as a Function of Concentration in a Transition Alloy*, Phys. Rev. Lett **53**, 687 (1984).

84. T. P. C. Klaver, R. Drautz, and M. W. Finnis, *Magnetism and thermodynamics of defect-free Fe-Cr alloys*, Physical Review B **74**, 094435 (2006).

85. A. Caro, D. A. Crowson, and M. Caro, *Classic many body potential for concentrated alloys, and the inversion of order in Fe-Cr*, Phys. Rev. Lett **95(7)**, 075702 (2005).

86. K. Vörtler, C. Björkas, D. Terentyev, L. Malerba, and K. Nordlund, *The effect of Cr concentration on radiation damage in Fe-Cr alloys*, J. Nucl. Mater. **382**, 24 (2008).

87. K. O. E. Henriksson and K. Nordlund, *Simulations of cementite: An analytical potential for the Fe-C system*, Phys. Rev. B **79**, 144107 (2009).

88. G. Janeschitz, ITER JCT, and HTs, *Plasma-wall interaction issues in ITER*, Journal of Nuclear Materials **290-293**, 1 (2001).

89. A. Loarte, *Implications of the use of Carbon-Based Plasma Facing Components in Next Step Fusion Devices*, Physica Scripta **T111**, 13 (2004).

90. R. Behrisch and W. Eckstein (ed.), *Sputtering by Particle Bombardment: Experiments and Computer Calculations from Threshold to MeV Energies* (Springer, Berlin, 2007).

91. J. Roth, *Chemical erosion of carbon based materials in fusion devices*, Journal of Nuclear Materials **266-269**, 51 (1999).

92. E. Salonen, K. Nordlund, J. Keinonen, and C. H. Wu, *Swift chemical sputtering of amorphous hydrogenated carbon*, Phys. Rev. B **63**, 195415 (2001).

93. K. Nordlund, E. Salonen, A. V. Krasheninnikov, and J. Keinonen, *Swift chemical sputtering of covalently bonded materials*, Pure and Applied Chemistry **78**, 1203 (2006).

94. J. F. Ziegler, sRIM-2008 software package, available online at *http://www.srim.org*.

95. G. Duxbury, M. F. Stamp, and H. Summers, *Observations and modelling of diatomic molecular spectra from JET*, Plasma Phys. Control. Fusion **40**, 361 (1998).

96. D. Nishijima, R. Doerner, M. J. Baldwin, G. De Temmerman, and E. M. Hollmann, *Properties of BeD molecules in edge plasma relevant conditions*, Plasma Phys. Control. Fusion **50**, 125007 (2008).

97. R. Doerner, M. J. Baldwin, D. Buchenauer, G. De Temmerman, and D. Nishijima, *The role of beryllium deuteride in plasma-beryllium interactions*, Journal of Nuclear Materials **390-391**, 681 (2009).

98. J. P. Sharpe, D. A. Petti, and H.-W. Bartels, *A review of dust in fusion devices: Implications for safety and operational performance*, Fusion Engineering and Design **63-64**, 153 (2002).

99. R. Parker, G. Janeschitz, H. Pacher, D. Post, S. Chiocchio, G. Federici, P. Ladd, I. J. C. Team, and H. Teams, *Plasma-wall interactions in ITER*, Journal fo Nuclear Materials **241-243**, 1 (1997).

100. J. Roth *et al.*, *Recent analysis of key plasma wall interactions issues for ITER*, Journal of Nuclear Materials **390-391**, 1 (2009).

101. J. Strachan, J. Likonen, P. Coad, M. Rubel, A. Widdowson, M. Airila, P. Andrew, S. Brezinsek, G. Corrigan, H. Esser, S. Jachmich, A. Kallenbach, A. Kirschner, A. Kreter, G. M. ans V. Phillips, R. Pitts, J. Spence, and M. Stamp, *Modelling of carbon migration during JET* ^{13}C *injection experiments*, Nuclear Fusion **48**, 105002 (2008).

102. G. Federici, *Plasma wall interactions in ITER*, Physica Scripta Volume T **124**, 1 (2006).

103. R. P. Doerner, M. Baldwin, J. Hanna, C. Linsmeier, D. Nishijima, R. Pugno, J. Roth, K. Schmid, and A. Wiltner, *Interaction of beryllium containing plasma with ITER materials*, Physica Scripta Volume T **128**, 115 (2007).

104. R. P. Doerner, *The implications of mixed-material plasma-facing surfaces in ITER*, Journal of Nuclear Materials **363-365**, 32 (2007).

105. P. Träskelin, C. Björkas, N. Juslin, K. Vörtler, and K. Nordlund, *Radiation damage in WC studied with MD simulations*, Nucl. Instr. Meth. Phys. Res. B **257**, 140103 (2006).

106. K. Ehrlich, E. Bloom, and T. Kondo, *International strategy for fusion materials development*, Journal of Nuclear Materials **283-287**, 79 (2000).

107. K. Nordlund, M. Ghaly, R. S. Averback, M. Caturla, T. Diaz de la Rubia, and J. Tarus, *Defect production in collision cascades in elemental semiconductors and FCC metals*, Phys. Rev. B **57**, 7556 (1998).

108. M. Ghaly, K. Nordlund, and R. S. Averback, *Molecular dynamics investigations of surface damage produced by keV self-bombardment of solids*, Phil. Mag. A **79**, 795 (1999).

109. K. Nordlund, *Molecular dynamics simulation of ion ranges in the 1 – 100 keV energy range*, Comput. Mater. Sci. **3**, 448 (1995).